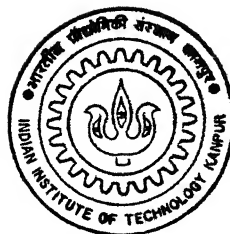


REGION OF INTEREST TOMOGRAPHY USING 1D MULTIREOLUTION ANALYSIS

by

Gomathi Sankar. S.

TH
CE/1996/m
G 5848



DEPARTMENT OF ELECTRICAL ENGINEERING

INDIAN INSTITUTE OF TECHNOLOGY KANPUR

March, 1996

EA
1996
M
GOM
RAG

REGION OF INTEREST TOMOGRAPHY USING 1D MULTIREOLUTION ANALYSIS

A Thesis Submitted

in Partial Fulfilment of the Requirements

for the Degree of

MASTER OF TECHNOLOGY

by

GOMATHI SANKAR. S.

to the

DEPARTMENT OF ELECTRICAL ENGINEERING

INDIAN INSTITUTE OF TECHNOLOGY KANPUR

March 1996

17 MAY 1986

CEN : LIBRARY
KANFIJR

100 No. A. 121551



A121551

EE-1996-M-GOM-REG

CERTIFICATE

It is certified that the work contained in the thesis titled Region of Interest Tomography Using 1D Multiresolution Analysis, by Gomathi Sankar. S. has been carried out under my supervision and that this work has not been submitted elsewhere for a degree.

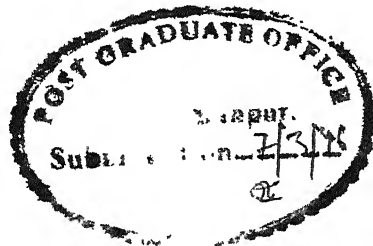
7th Mar, 1996


Dr. Sumana Gupta

Associate Professor,

Department of Electrical Engineering

IIT, Kanpur.



ABSTRACT

In this thesis Region of Interest Image Reconstruction from Projections using Wavelet transform has been studied. The convolution backprojection operator, used for reconstruction of images from projections, has a non-local filter which requires global projection data. This increases the objects' exposure time to harmful radiation. It is proved that this filtering operation can be done on the chosen wavelet function instead of the projections. This localizes the filter and leads to the region of interest image reconstruction. In this thesis one-dimensional multiresolution analysis is used for region of interest image reconstruction and verified through simulations using computer generated images. The performance of the algorithm is compared with the other reported algorithms.

Contents

1	Introduction	1
1.1	Review	1
1.2	Organization of the Thesis	2
2	Mathematical Preliminaries	3
2.1	Image Reconstruction from Projections	3
2.1.1	Radon Transform And Some Of Its Properties	3
2.1.2	Inverse Radon Transform	5
2.2	Wavelet Transform	8
2.2.1	Continuous Wavelet Transform	8
2.2.2	Discrete Parameter Wavelet transform	9
2.2.3	Discrete Time Wavelet Transform and Discrete Wavelet Transform	11
2.2.4	DPWT and multiresolution Analysis	11
3	ROI Reconstruction Using Wavelets	15
3.1	Wavelet Localization of The Radon Transform	15
3.1.1	Nonlocality Of $ \xi \hat{W}(\xi)$	15
3.1.2	Wavelet Localization Of $ \xi \hat{W}(\xi)$	16
3.2	Localization Of $ \xi \hat{W}(\xi)$ With 2D MRA Reconstruction	17
3.2.1	Multiresolution Reconstruction With 2D MRA	18
3.2.2	ROI Reconstruction With 2D MRA	19
3.3	Mutiresolution Reconstruction Using 1D Wavelets	21
3.4	1D MRA in Multiresolution Reconstruction	22
3.4.1	Single Level MRA With CBP	22

3.4.2	Determination of 2D filters	23
3.4.3	Properties of the Constructed 2D filters	24
3.4.4	Higher level Decomposition	25
3.4.5	Region of Interest Reconstruction	26
4	Implementation and Discussions	30
4.1	Simulation Results	30
4.2	Discussions	32
4.3	Comparison of the Algorithms	32
4.3.1	Aliasing effect	33
4.3.2	Computational Complexity	35
5	Conclusion	53

List of Figures

2.1	Schematic for Radon transform operation	4
2.2	Various $ \xi \hat{W}(\xi)$ filters. (a) Ram-Lak. (b) Shepp-Logan. (c) Lowpass cosine. (d) Generalized Hamming.	7
2.3	Computing wavelet coefficients through subband technique . .	13
2.4	Inverse wavelet transform through subband techniques	13
3.1	A simple combination of CBP and MRA.	18
3.2	Modification of the simple ‘CBP-MRA’ combination by mov- ing CBP inside.	19
3.3	Tiling of the frequency plane by the 2D wavelet transform, and the central slice used in the modified 1D filter.	20
3.4	A simple combination of 1D MRA and CBP.	22
3.5	Modification of the simple ‘MRA-CBP’ combination by mov- ing CBP inside.	23
3.6	Tiling of the frequency plane by the constructed 2D wavelet transform.	24
3.7	An equivalent implementation of MRA.	25
3.8	Tiling of the frequency plane by the constructed 2D wavelet transform.	26
3.9	Multiresolution reconstruction for three level MRA.	27
3.10	Region of reconstruction for three level MRA.	29
4.1	Sampling scheme for the region of interest reconstruction inputs.	31
4.2	The aliasing effect produced in 2D MRA reconstruction for a particular angle θ	33

4.3	The aliasing effect produced in 2D MRA reconstruction shown in two-dimensional frequency plane.	34
4.4	Shepp-Logan Phanthom head image used for simulations. . . .	36
4.5	Frequency responses of the 1D analysis filters.	36
4.6	Frequency response of the 2D synthesis filter $h(n_1, n_2)$ constructed with misaligned scaling function.	37
4.7	Frequency response of the 2D synthesis filter $g(n_1, n_2)$	38
4.8	Frequency response of the 2D synthesis filter $hg(n_1, n_2)$	39
4.9	Frequency response of the 2D synthesis filter $hhg(n_1, n_2)$	40
4.10	Frequency response of the 2D synthesis filter $hhhh(n_1, n_2)$	41
4.11	Illustration of the effect of misalignment of projection origin. . .	42
4.12	Multiresolution reconstruction: Image at resolution 2^{-1}	43
4.13	Multiresolution reconstruction: Image at resolution 2^{-2}	43
4.14	Multiresolution reconstruction: Image at resolution 2^{-3}	44
4.15	Multiresolution reconstruction: Coarse image at resolution 2^{-3} . . .	44
4.16	Multiresolution reconstruction: Overall added image.	44
4.17	Frequency response of the 2D synthesis filter $g_R(n_1, n_2)$	45
4.18	Frequency response of the 2D synthesis filter $hg_R(n_1, n_2)$	46
4.19	Frequency response of the 2D synthesis filter $hhg_R(n_1, n_2)$. . .	47
4.20	Centered region of interest image at resolution 2^{-1}	48
4.21	Centered region of interest image at resolution 2^{-2}	48
4.22	Centered region of interest image at resolution 2^{-3}	49
4.23	Region of interest reconstruction: Coarse image at resolution 2^{-3}	49
4.24	Overall added centered region of interest image.	49
4.25	Offcentered region of interest image at resolution 2^{-1}	50
4.26	Offcentered region of interest image at resolution 2^{-2}	50
4.27	Offcentered region of interest image at resolution 2^{-3}	51
4.28	Overall added offcentered region of interest image.	51
4.29	Computational requirements in number of multiplications for the varying region of interest samples.	52

Chapter 1

Introduction

1.1 Review

One of the conventional techniques used for the two-dimensional image reconstruction from its projections is the method of convolution back projection. In this method projections are filtered with a non-local filter which requires global projection data. Recently a new approach using wavelets has been reported in [9, 10], [13]-[18]. In reference [9], a wavelet localization of Radon transform is carried out and it is shown that wavelets with several zero moments localizes the ramp filter used in convolution backprojection. This led a new approach for region of interest reconstruction of an image.

Considering the drawbacks of the algorithm given in [9], Daleney *et.al.* proposed a new algorithm using the two-dimensional multiresolution analysis. The main goal of their algorithm is to reconstruct the image at various levels and a simple modification in the scheme results in the region of interest image reconstruction with reduced exposure. By introducing a set of angle dependent filters, derived from the 2D-MRA analysis filters, the convolution backprojection operation is shifted inside the 2D-MRA. The angle dependent filters are now combined with the non-local filters to obtain local filters. With this combined filters the region of interest is made possible. This is verified by simulation.

In [11], the reconstruction of an image from one-dimensional wavelet

transform of the projections has been studied. It has been proved that inverse Radon transform of wavelet transform of the projections at a particular scale is the two-dimensional wavelet transform of the given image. The two-dimensional wavelet is the inverse Radon transform of the one-dimensional wavelet operated on the projections. The algorithm was implemented in Fourier domain.

In the present thesis work one-dimensional multiresolution analysis has been used for image reconstruction at various resolution levels and for region of interest image reconstruction. The underlying theory has been worked out in detail and explained with illustrative figures. The computer generated Shepp-Logan phantom head has been used for implementing the algorithm and the results are discussed. The limitations of the proposed algorithm has been analyzed using the results obtained.

1.2 Organization of the Thesis

The thesis is organized as follows.

- In chapter 2, the relevant results from Radon transform and Wavelet transform are reviewed.
- In chapter 3, the reported works are reviewed briefly and the proposed algorithm is explained in detail.
- In chapter 4, the practical difficulties in implementing the algorithm is discussed. The simulation results for the computer generated images are shown. A discussion of the limitations of the algorithm is given. A comparison of our algorithm with the previously reported algorithms are given.
- In chapter 5, we conclude the thesis with summarizing the algorithm's performance.

Chapter 2

Mathematical Preliminaries

This chapter briefly reviews the mathematical preliminaries used in forthcoming chapters. For detailed treatment about Radon transform readers are referred to [2] and [1], and for wavelets to references [5], [3], [6], and [4].

2.1 Image Reconstruction from Projections

Image reconstructions from projections is the process of producing an image of a two-dimensional distribution (of some physical property) from the estimates of its line integral along a finite number of lines at known locations. The basic mathematical framework common to a large class of such reconstruction problem was first developed by Johann Radon, and is referred to as Radon transform. Radon transform is a process which maps an n -dimensional function in Euclidean space \mathcal{R}^n to a set of $n - 1$ -dimensional functions in Euclidean space \mathcal{R}^{n-1} , along all possible angles. Here we restrict ourselves to Radon transform and its inverse for two-dimensional functions only.

2.1.1 Radon Transform And Some Of Its Properties

Definition : Let (x, y) designate coordinates of a point in a plane. Consider an arbitrary function $f(x, y)$ defined over some domain D in \mathcal{R}^2 . Then its Radon transform (also known as the projections), $p(s, \theta)$ is given by

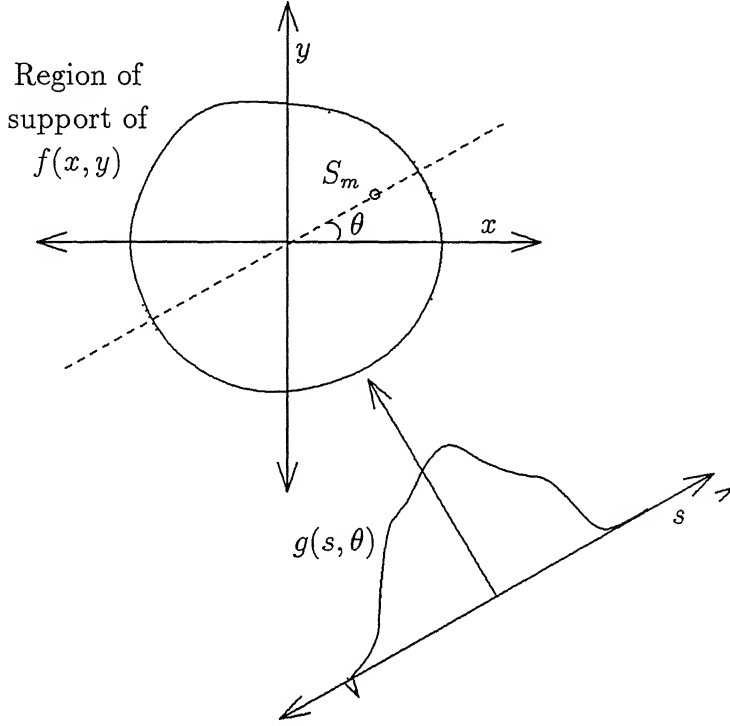


Figure 2.1: Schematic for Radon transform operation

$$p(s, \theta) = \int_{-\infty}^{\infty} \int_{-\infty}^{\infty} f(x, y) \delta(x \cos \theta + y \sin \theta - s) dx dy \quad (2.1)$$

If f is continuous and has compact support, then $p(s, \theta)$ uniquely determines $f(x, y)$ [1].

The function $p(s, \theta)$ at any particular value s and θ is the line integral along the line $s = x \cos \theta + y \sin \theta$. In eqn. (2.1) $\delta(\cdot)$ is Dirac delta function, defined as

$$\delta(x) = \begin{cases} 1 & \text{if } x = 0 \\ 0 & \text{if } x \neq 0 \end{cases} \quad (2.2)$$

Fig. 2.1 illustrates the way a two-dimensional function or image $f(x, y)$ is mapped to $p(s, \theta)$. Practically $p(s, \theta)$ is found only for finite number of angles and finite number of samples in region of support.

Some properties of the Radon transform which we will refer to in this work are given below. In the following properties, let $p(s, \theta)$, $p_1(s, \theta)$ and $p_2(s, \theta)$ represent the Radon transform of the functions $f(x, y)$, $f_1(x, y)$ and $f_2(x, y)$

respectively. $\hat{p}(\xi, \theta)$ is the Fourier transform of $p(s, \theta)$ and $\hat{F}(\xi_1, \xi_2)$ is the two-dimensional Fourier transform of $f(x, y)$.

1. *Projection Slice theorem* : The one-dimensional Fourier transform on s of $p(s, \theta)$ is equal to the central slice, at an angle θ of the two-dimensional Fourier transform of the object $f(x, y)$.

$$\hat{p}(\xi, \theta) = \hat{F}(\xi \cos \theta, \xi \sin \theta) \quad (2.3)$$

2. Radon transform is linear, i.e., given the scalars, $a_1, a_2 \in \mathcal{R}$, we have,

$$a_1 f_1(x, y) + a_2 f_2(x, y) \xrightarrow{\text{R.T}} a_1 p_1(s, \theta) + a_2 p_2(s, \theta)$$

3. *Convolution property* : The Radon transform of the two-dimensional convolution of two two-dimensional signals $f_1(x, y)$ and $f_2(x, y)$ is the one-dimensional convolution of the Radon transform of the two signals.

$$f_1(x, y) \otimes_2 f_2(x, y) \xrightarrow{\text{R.T}} p_1(s, \theta) \otimes_1 p_2(s, \theta) \quad (2.4)$$

where \otimes_1 represents one-dimensional convolution on 's', \otimes_2 represents two-dimensional convolution and R.T represents the Radon transform operation.

2.1.2 Inverse Radon Transform

Several inverse operations for obtaining the two-dimensional function from its projections, are reported in literature (refer [2] for them). Among them we consider only a particular method known as *convolution back projection*. Connected with that is the Back projection operator which operates on the projection $p(s, \theta)$ to give a function $b(x, y)$ as

$$b(x, y) = \int_0^\pi p(x \cos \theta + y \sin \theta, \theta) d\theta \quad (2.5)$$

Back projection represents the accumulation of the ray sums of all the rays that pass through the point (x, y) . Backprojection operator is not the inverse

of the Radon transform but the inverse Radon transform operation involves this operator. The inverse Radon transform is,

$$f(x, y) = \frac{1}{4\pi^2} \int_0^\pi \int_{-\infty}^{\infty} |\xi| \hat{p}(\xi, \theta) e^{j\xi(x\cos\theta + y\sin\theta)} d\xi d\theta \quad (2.6)$$

where $\hat{p}(\xi, \theta)$ is the one-dimensional Fourier transform of $p(s, \theta)$ with respect to 's'. We note that in equation (2.6), the inner integral represents the inverse Fourier transform of $|\xi| \hat{p}(\xi, \theta)$, i.e., it represents the filtering of the projections $p(s, \theta)$ with the ramp filter whose frequency response is $|\xi|$. The outer integral represents the backprojection operation on these filtered projection.

In discrete domain implementation, $|\xi|$ needs to be sampled to obtain a discrete filter. Since $|\xi|$ is of infinite bandwidth and the value at higher frequency is much larger than at lower frequency, the aliasing effect will be enormous. This leads to bandlimiting $|\xi|$ before sampling it. The window used is rectangular window called the Ram-Lak filter.

The Ram-Lak filter amplifies the high frequency components of the projections. Since the noise strength in the high frequency region is generally more than the signal strength, we use a window with a gentle roll off characteristics to avoid the ringing at the edges. The characteristics of some functions that are normally used along with $|\xi|$ are given below

1. Ram-Lak

Frequency response	$H_{\text{RL}}(\xi) = \xi \text{rect}(\xi d)$
Impulse response	$h_{\text{RL}}(s) = \xi_0^2 [2\text{sinc}(2\xi_0 s) - \text{sinc}^2(\xi_0 s)]$
Discrete impulse response	$h_{\text{RL}}(m) = \begin{cases} \frac{1}{4d}, & m = 0 \\ \frac{-\sin^2(\pi m/2)}{\pi^2 m^2 d} & m \neq 0 \end{cases}$

2. Shepp-Logan

Frequency response	$H_{\text{SL}}(\xi) = \xi \text{sinc}(\xi d) \text{rect}(\xi d)$
Impulse response	$h_{\text{SL}}(s) = \frac{2(1 + \text{sinc} 2\pi \xi_0 s)}{\pi^2 (d^2 - 4s^2)}$
Discrete impulse response	$h_{\text{SL}}(m) = \frac{2}{\pi d(1 - 4m^2)}$

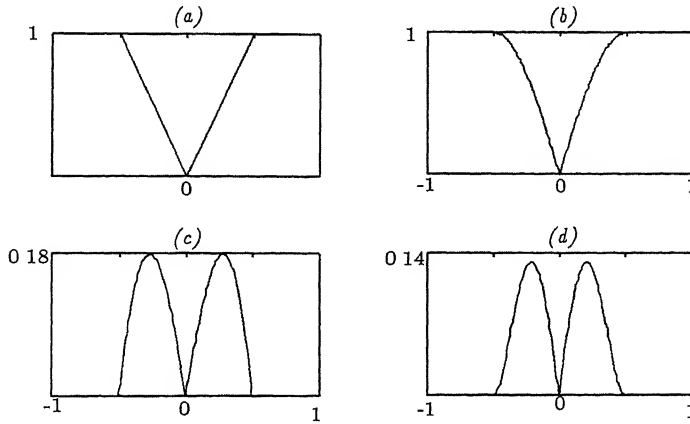


Figure 2.2: Various $|\xi|\hat{W}(\xi)$ filters. (a) Ram-Lak. (b) Shepp-Logan. (c) Lowpass cosine. (d) Generalized Hamming.

3. Low-pass cosine

$$\begin{aligned}
 \text{Frequency response} \quad H_{\text{LP}}(\xi) &= |\xi| \cos(\pi \xi d) \text{rect}(\xi d) \\
 \text{Impulse response} \quad h_{\text{LP}}(s) &= \frac{1}{2} \left[h_{\text{RL}}\left(s - \frac{d}{2}\right) + h_{\text{RL}}\left(s + \frac{d}{2}\right) \right] \\
 \text{Discrete impulse response} \quad h_{\text{LP}}(m) &= \frac{1}{2} \left[h_{\text{RL}}\left(m - \frac{1}{2}\right) + h_{\text{RL}}\left(m + \frac{1}{2}\right) \right]
 \end{aligned}$$

4. Generalized Hamming for an $\alpha : 0 \leq \alpha \leq 1$

$$\begin{aligned}
 \text{Frequency response} \quad H_{\text{H}}(\xi) &= \\
 &|\xi| [\alpha + (1 - \alpha) \cos(2\pi \xi d)] \text{rect}(\xi d) \\
 \text{Impulse response} \quad h_{\text{H}}(s) &= \\
 &\alpha h_{\text{RL}}(s) + \frac{1-\alpha}{2} [h_{\text{RL}}(s - d) + h_{\text{RL}}(s + d)] \\
 \text{Discrete impulse response} \quad h_{\text{H}}(m) &= \\
 &\alpha h_{\text{RL}}(m) + \frac{1-\alpha}{2} [h_{\text{RL}}(m - 1) + h_{\text{RL}}(m + 1)]
 \end{aligned}$$

An additional problem associated with the $|\xi|\hat{W}(\xi)$ is the need for filters with large lengths in spatial domain. This is so because each of these filters is non-differentiable at the origin of the frequency domain. The consequences of this and related effects are discussed in chapter 3.

2.2 Wavelet Transform

Wavelets are relatively recent development in applied mathematics. The concept can be viewed as a synthesis of ideas which originated in diverse areas such as, physics, engineering, and pure mathematics. As a result, wavelets appeal to engineers as well as to scientists. Image coding, speech processing, coherent state study in physics, are but few of the applications of wavelets. Since there are four different types of wavelet transforms and as there are yet no standard names for them, the terminology in the literature can at times be confusing. We adapt the terminology used in [5].

2.2.1 Continuous Wavelet Transform

The Fourier transform of a given signal gives the frequency content of the signal. However it fails to provide information about the time evolution of the frequency content, i.e., how the frequency contents of the given signal change with time. This time-frequency localization is achieved by the wavelet transform. The wavelet transform of signal $f(t)$ evolving in time depends on two variables, scale 'a' and time 'b'.

$$(\text{CWT}_\psi f)(a, b) = \frac{1}{|a|^{1/2}} \int_{-\infty}^{\infty} f(t) \psi \left(\frac{t-b}{a} \right) dt \quad (2.7)$$

where $\psi(t)$ is the mother wavelet function which satisfies the admissibility condition given by

$$C_\psi = 2\pi \int_{-\infty}^{+\infty} \frac{|\hat{\psi}(\xi)|^2}{|\xi|} d\xi < \infty \quad (2.8)$$

where $\hat{\psi}(\xi)$ is the Fourier transform of $\psi(t)$. This requires

$$\int_{-\infty}^{\infty} \psi(t) dt = 0$$

and

$$|\hat{\psi}(\xi)| < \infty.$$

When the wavelet function satisfies above condition, the inverse wavelet transform exists and is given by

$$f(t) = \frac{1}{C_\psi} \int_{-\infty}^{\infty} \int_{-\infty}^{\infty} (\text{CWT}_\psi f)(a, b) \psi \left(\frac{t-b}{a} \right) \frac{1}{|a|^{1/2} a^2} da db \quad (2.9)$$

The scaling used in the wavelet transform zooms into the short lived high frequency signals or zooms out the lengthy low frequency signal, by varying width of the support of the function $\psi(t)$. This property of the wavelet transform distinguishes it from other time frequency analysis techniques such as the windowed Fourier Transform or STFT.

2.2.2 Discrete Parameter Wavelet transform

In eqn. (2.10), both ‘ a ’ and ‘ b ’ are continuous variables and there is a redundancy in the representation. The function $f(t)$ can be recovered from $(W_\psi f)(a, b)$; for discrete values of a, b , if they are sampled sufficiently dense to satisfy the Nyquist criterion. As most of the common signals have short lived high frequency components and lengthy low frequency components, sampling the variables ‘ a ’ and ‘ b ’ will be optimal if ‘ a ’ is sampled in log scale and ‘ b ’ is made proportional to ‘ a ’ [4], i.e. $a = a_0^m$ and $b = nb_0 a_0^m$. So the discrete parameter wavelet transform is defined as

$$(\text{DPWT}_\psi f)(m, n) = \frac{1}{a_0^{m/2}} \int_{-\infty}^{\infty} f(t) \psi(a_0^{-m}t - nb_0) dt \quad (2.10)$$

This can also be written as

$$(\text{DPWT}_\psi f)(m, n) = \int f(t) \psi_{mn}(t) dt, \quad (2.11)$$

where $\psi_{mn}(t) = 2^{-m/2} \psi(2^{-m}t - n)$. It is of interest to study different wavelet functions $\psi(t)$, and the constants a_0 and b_0 that permit perfect reconstruction (see the discussion in next paragraph also) of the function $f(t)$. That is,

$$f(t) = \sum_{m,n} (\text{DPWT}_\psi f)(m, n) \psi_{mn}(t). \quad (2.12)$$

Suppose there is over sampling on a and b , then eqn. (2.12) will not only hold but moreover, it is possible to have a non-unique representation of $f(t)$, with respect to the same $\psi(t)$ [5].

The oversampling of the variables a and b leads to a new approach, representation of $f(t)$ with non-orthonormal functions. The theory of frames in vector space is a generalization of the orthonormal decomposition of

functions, which includes non-orthonormal decompositions also. In an n -dimensional vector space V , a set of vectors $\{v_i\}$; $i = 1$ to m ; $m \leq n$ is considered. Any vector $x \in V$ is decomposed by $\{v_i\}$ to the inner product of x with every v_i , represented as $\langle x, v_i \rangle$. The set $\{v_i\}$ forms a frame in vector space V if and only if, for any non-zero vector $x \in V$,

$$A\|x\|^2 \leq \sum_{i=1}^m |\langle x, v_i \rangle|^2 \leq B\|x\|^2 \quad (2.13)$$

where A and B are constants, dependent on $\{v_i\}$ only, called frame bounds, with $0 < A \leq B < \infty$. For a frame $\{v_i\}$, a dual frame $\{\bar{v}_i\}$ can be found so that any vector $x \in V$ can be obtained back exactly from its decomposition by $\{v_i\}$, as given by,

$$x = \sum_{i=1}^m \langle x, v_i \rangle \bar{v}_i. \quad (2.14)$$

Some basic results from the theory of frames are listed below.

1. A frame is *tight* if $A = B$.
2. If removal of a single element in a tight frame violates the lower bound of eqn. 2.13 then the tight frame is an *exact frame*.
3. Elements of a tight, exact frame with $A = B = 1$ form an *orthonormal basis*.

Eqn. (2.12) is a special case and another possible perfect reconstruction of the signal from eqn. (2.11) is also available. If $\psi_{mn}(t)$ are elements of a frame then a dual frame $\bar{\psi}_{mn}(t)$ can be found such that

$$f(t) = \sum_{m,n} (\text{DPWT}_\psi f)(m,n) \bar{\psi}_{mn}(t). \quad (2.15)$$

If $\psi_{mn}(t)$ forms a frame, it obeys the inequality

$$A\|f(t)\|^2 \leq \sum_m \sum_n |\langle f(t), \psi_{mn}(t) \rangle|^2 \leq B\|f(t)\|^2 \quad (2.16)$$

with $0 < A \leq B < \infty$. The constants A and B are frame bounds and are dependent only on $\psi_{mn}(t)$, and

$$\|f(t)\|^2 = \int |f(t)|^2 dt < \infty.$$

For some very special choice of ψ , a_0 and b_0 , it has been proved that if we choose $a_0 = 2$ and $b_0 = 1$ then $\{\psi_{mn} : m, n \in \mathbb{Z}\}$ constitutes an orthonormal basis of $L^2(\mathcal{R})$ ([3]). Amongst these functions, Daubechies orthonormal wavelets are well known and often used. In this thesis we use Daubechies orthonormal wavelets for simulation purpose.

2.2.3 Discrete Time Wavelet Transform and Discrete Wavelet Transform

For discrete time signals two different types of wavelet transforms are defined. One is the discrete time wavelet transform defined as,

$$(\text{DTWT } f)(m, n) = a_0^{-m/2} \sum_k f(k) \psi(a_0^{-m} k - n b_0). \quad (2.17)$$

This is time discretization of the discrete parameter wavelet transform. The other transform is the discrete wavelet transform defined as,

$$(\text{DWT } f)(m, n) = 2^{-m/2} \sum_k f(k) \psi(2^{-m} k - n), \quad (2.18)$$

where the discrete wavelet function $\psi(k)$ can be, but need not necessarily, a sampled version of its continuous counterpart. For detailed analysis of these two transforms readers are referred to [3, 5].

2.2.4 DPWT and multiresolution Analysis

The idea of multiresolution analysis is very similar to dyadic subband decomposition and coding. In that, a lowpass filter $\tilde{h}(n)$ and a highpass filter $\tilde{g}(n)$ operates separately on the signal. After decimation by 2, the signal is decomposed into subband components. The same scheme is repeated on the lowpass output of the previous level to obtain the next level decomposition. It is well known that with proper choice of $\tilde{h}(n)$ and $\tilde{g}(n)$ filters the signal can be perfectly reconstructed with upsampling and $h(n)$ and $g(n)$ at every level [12]. This is related to discrete parameter wavelet transform decomposition. The theory developed by Mallat [6] is briefly reviewed below.

A sequence of vector spaces $\{V_j : j \in \mathcal{Z}\}$ is said to be a Multiresolution Analysis of $L^2(\mathcal{R})$ if they satisfy the following properties and the theorems stated below [6].

- i. $\dots \subset V_2 \subset V_1 \subset V_0 \subset V_{-1} \subset V_{-2} \subset \dots$
- ii. $\bigcup_{j \in \mathcal{Z}} V_j = L^2(\mathcal{R})$
- iii. $\bigcap_{j \in \mathcal{Z}} V_j = \{0\}$
- iv. if $f(t) \in V_j$ then $f(2^j t) \in V_0$
- v. if $f(t) \in V_0$ then $f(t - k) \in V_0$ for $k \in \mathcal{Z}$

Theorem : 1 For a given multiresolution analysis of $L^2(\mathcal{R})$, there exists a function $\phi(t)$ such that $\{\phi_{mn}(t) : n \in \mathcal{Z}\}$ forms a basis of V_m , where $\phi_{mn}(t) = 2^{-m/2} \phi(2^{-m}t - n)$. The function $\phi(t)$ is unique and is referred to as a scaling function.

Theorem : 2 Associated with each MRA, is a unique orthonormal wavelet function $\psi(t)$.

Any signal $f(t) \in L^2(\mathcal{R})$ is projected onto the vector space V_0 by

$$s(n) = \int f(t) \phi(t - \lambda) \Big|_{\lambda=nT} dt \quad (2.19)$$

This $\hat{f}(n)$ is decomposed using filter $\tilde{g}(n)$ to get discrete parameter wavelet transform of $f(t)$ at 2^{-1} level. The decomposition by $\tilde{h}(n)$ results in the projection of $f(t)$ onto V_1 , denoted as c_1 . Further decomposition of c_1 with $\tilde{g}(n)$ and $\tilde{h}(n)$ results in c_n and discrete parameter wavelet transform of $f(t)$ at 2^{-n} level.

The filters $\tilde{g}(n)$ and $\tilde{h}(n)$ are related to wavelet and scaling functions and given by,

$$h(n) = \frac{1}{2} \int \phi(t) \phi(2t - n) dt \quad (2.20)$$

$$g(n) = \frac{1}{2} \int \psi(t) \phi(2t - n) dt, \quad (2.21)$$

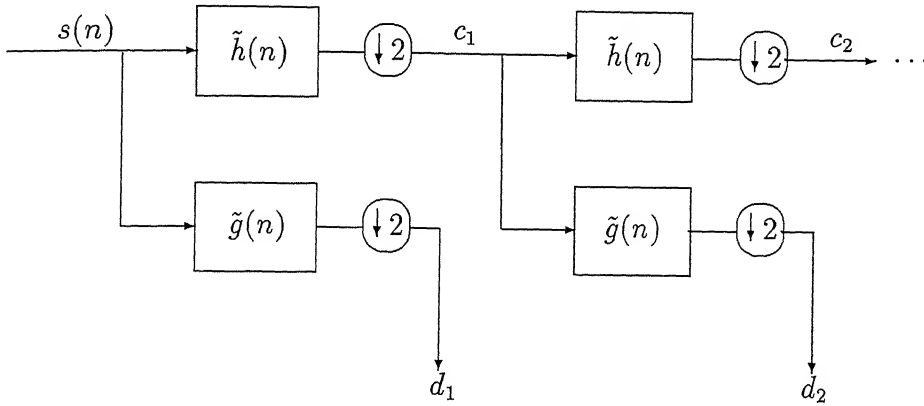


Figure 2.3: Computing wavelet coefficients through subband technique

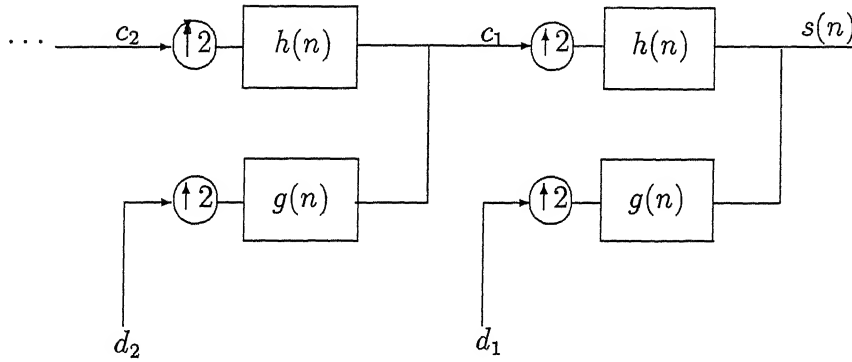


Figure 2.4: Inverse wavelet transform through subband techniques

and

$$\phi(t) = 2 \sum_{l=0}^{p-1} h(l) \phi(2t - l) \quad (2.22)$$

$$\psi(t) = 2 \sum_{l=0}^{p-1} g(l) \phi(2t - l). \quad (2.23)$$

From the above theory it is noted that

$$d_k(n) = \int f(t) \psi_{kn}(t) dt. = \text{DPWT}_{\psi}(k, n) \quad (2.24)$$

Eqn. (2.24), gives a simple algorithm to obtain discrete parameter wavelet transform of the signal. The decomposition scheme is shown in Fig. 2.3. The reconstruction scheme is given in Fig. 2.4.

In practice discrete time signals are needed to be analyzed rather than continuous time signals. So the discrete time signal is assumed as $f(n)$. As long as we can reproduce $f(n)$, the corresponding $f(t)$ is not coming in to the picture. In this thesis we use this multiresolution analysis for discrete parameter wavelet transform using Daubechies-10 compactly supported wavelet.

Chapter 3

ROI Reconstruction Using Wavelets

In this chapter we consider the region of interest reconstruction from minimum possible projections. This problem has been considered and tried out by few authors also in different ways [13]-[18],[10, 9]. Among them we consider one particular method[9], which combines the non-local filter with wavelet function to obtain a local filter. In section 3.1 and 3.2 we review the methods from references [9] and [10] respectively. Section 3.3 reviews the theory of reference [11]. Section 3.4 discusses the proposed algorithm.

3.1 Wavelet Localization of The Radon Transform

In this section, the reason for the non-locality of the filter $|\xi|\hat{W}(\xi)$ is first analysed. The method to overcome this problem, as given in [9], is briefly discussed.

3.1.1 Nonlocality Of $|\xi|\hat{W}(\xi)$

As mentioned in the chapter 2. the filter $|\xi|\hat{W}(\xi)$ is not locally supported. This stems from the fact that the function $|\xi|$ is not differentiable at the origin. The non-locality implies that local calculation of the convolution

in eqn. (2.6) will require global values of the Radon transform. The non-differentiability at the origin can not be significantly altered by the window $\hat{W}(\xi)$, without distorting the structure of the image.

Consider the convolution, (which is multiplication in the frequency domain) as a filter operation denoted by \mathcal{F} , and we will write it as a two step process. The first step is multiplication by $\imath\xi$ in the frequency domain (or differentiation in the time domain). The second step is the application of Hilbert transform H . Thus the filtering process is given by

$$\begin{aligned}\mathcal{F}\{f(x)\} &= \text{IFT}\left\{\frac{1}{\imath}\text{sign}(\xi)(\imath\xi)\hat{f}(\xi)\right\} \\ &= \text{IFT}\{|\xi|\hat{f}(\xi)\}.\end{aligned}\tag{3.1}$$

where

$$\text{sign}(\xi) = \begin{cases} 1 & \text{if } x \geq 0 \\ 0 & \text{if } x \leq 0. \end{cases}\tag{3.2}$$

The differentiation operation is local, but the Hilbert transform is not, since it imposes non-differentiability upon the Fourier transform of any smooth function whose average value is not zero.

3.1.2 Wavelet Localization Of $|\xi|\hat{W}(\xi)$

The imposition of non-differentiability at the origin in the frequency domain and the subsequent spreading of the support of the function, will not occur if the function's Fourier transform is zero at the origin and the function has several zero moments. But we can not impose conditions on the Radon transform of an image. The trick here is to combine the $|\xi|\hat{W}(\xi)$ filter with some other function which has the desired properties as well as provides a method of reconstruction with the combined filter. This can be done as follows.

Consider the convolution backprojection equation (2.6) given by,

$$f(x, y) = \int p(s, \theta) \otimes_{1D} \text{IFT}\{|\xi|\hat{W}(\xi)\} d\theta\tag{3.3}$$

$$= \int \mathcal{F}\{p(s, \theta)\} d\theta\tag{3.4}$$

$$= \int \mathcal{F}\left\{\sum_{m,n} c_{m,n}(\theta) \psi_{m,n}(s)\right\} d\theta \quad (3.5)$$

$$= \int \sum_{m,n} c_{m,n}(\theta) \mathcal{F}\{\psi_{m,n}(s)\} d\theta \quad (3.6)$$

This gives a novel reconstruction formula where the filtering is done on wavelet function. By choosing a wavelet function with several zero moments we can localize the $\mathcal{F}(\psi_{m,n}(s))$ and hence the inverse Radon transform. When $\psi_{m,n}(s)$ is compactly supported, $c_{m,n}(\theta)$ can be calculated using local information. In this algorithm to obtain the region of interest reconstruction the projections are taken along the region of interest with a small offset accounting for both the calculation of $c_{m,n}(\theta)$ and the inverse operation. Implementation of this is discussed in [9]. The major drawbacks [9, 10] in their algorithm are listed below.

1. Though, the reconstruction at the region of interest is good, the reconstructed image has severe artifacts outside the region of interest.
2. The algorithm is prone to aliasing error when the region of interest is off centered. The process of centering the projections before interpolation and reconstruction introduces this aliasing error.
3. It is not mentioned in the reference, how multiple non-concentric regions can be handled.

3.2 Localization Of $|\xi| \hat{W}(\xi)$ With 2D MRA Reconstruction

In [10], Delaney and Bresler uses the basic ideas from [9] and taking into consideration the algorithm's drawbacks, proposes a new algorithm which combines the filter with two-dimensional separable MRA analysis filters. Their algorithm is briefly discussed.

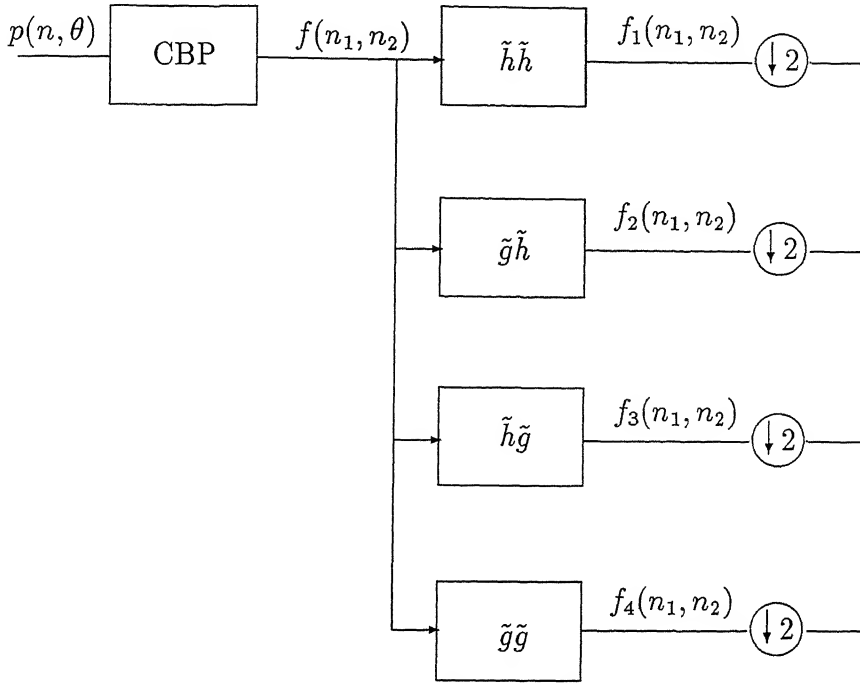


Figure 3.1: A simple combination of CBP and MRA.

3.2.1 Multiresolution Reconstruction With 2D MRA

Consider Fig. 3.1. Since the MRA gives perfect reconstruction $f(n_1, n_2)$ and the synthesised output will be exactly equal. The analysis is carried out in two-dimension as

$$f_1(n_1, n_2) = f(n_1, n_2) \otimes_{2d} \tilde{h}\tilde{h}(n_1, n_2) \quad (3.7)$$

By convolution property of Radon transform, the equation is modified to

$$f_1(n_1, n_2) = \text{IRT}\{p(n, \theta) \otimes_{1d} k_{hh}(n)\} \quad (3.8)$$

where,

$$k_{hh}(\theta, n) = \text{IFT}_{2d}\{\hat{h}(\xi \cos \theta)\hat{h}(\xi \sin \theta)\} \quad (3.9)$$

This modified scheme is shown in Fig. 3.2, in which ‘ k ’ blocks represents the one-dimensional angle dependent filters obtained from eqn. (3.9). The advantage of having this representation is that the convolution part of CBP can be now combined with the ‘ k ’ filters. As proved in [9], the combination

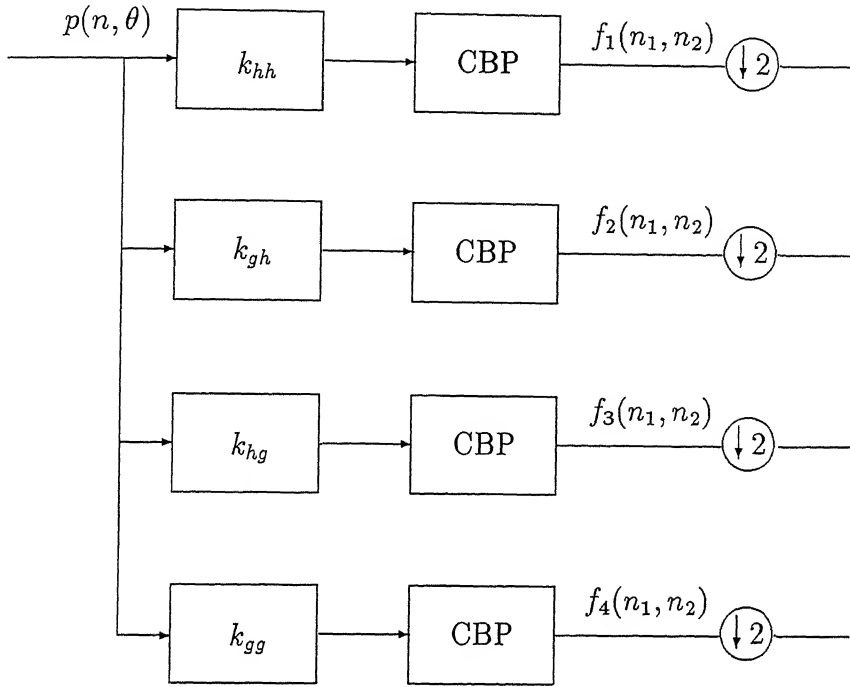


Figure 3.2: Modification of the simple ‘CBP-MRA’ combination by moving CBP inside.

will result in local filters if the filters have zero at the origin and in the neighbourhood of origin.

3.2.2 ROI Reconstruction With 2D MRA

By examining how the two-dimensional separable wavelet transform tiles the frequency plane, we can get a clear perception of the properties of the one-dimensional angle dependent filters. The tiling is shown in simplified form in Fig. 3.3. Note that spectra of actual filters overlap with each other to some extent. By the projection slice theorem, the one-dimensional filter at particular angle has a passband from $-\xi_\theta$ to ξ_θ . So for all θ the $k_{hh}(\theta, n)$ are lowpass filters. The reconstruction obtained from this particular channel is of very low bandwidth. This reduces the number of projection angles needed in Radon transform to a minimum. So projections taken at less number of angles are given to this channel, which means less exposure of the object to

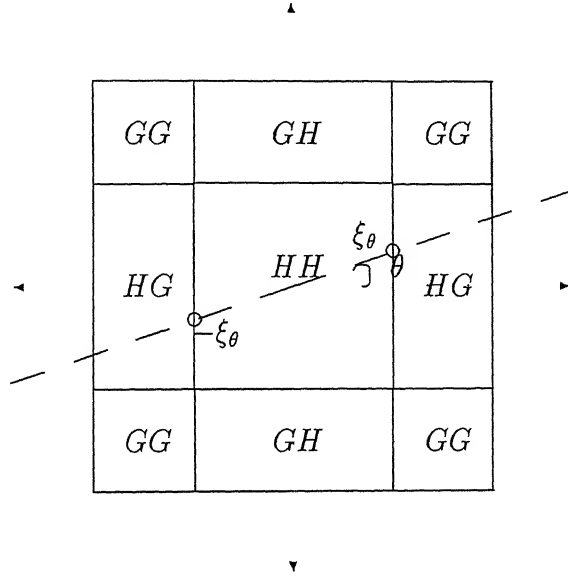


Figure 3.3: Tiling of the frequency plane by the 2D wavelet transform, and the central slice used in the modified 1D filter.

radiation.

On the contrary, other channels use high-pass filters of different nature each having zero at the origin of frequency plane and zero in the neighbourhood. So if we combine the function $|\xi|\hat{W}(\xi)$ with these filters they result in compactly supported filters as explained earlier. So with more angular sampling, the projections are taken only around region of interest with an offset accounting for the filter length. The over all algorithm is

- Find the angle dependent filters using eqn. (3.8).
- Convolve these filters with $|\xi|\hat{W}(\xi)$.
- Input the projections corresponding to a reduced number of angles to the lowpass channel.
- Input the projections at all angles around the region of interest to other channels.
- Backproject the data on all channels.

- Downsampling and upsampling is carried out along row and column.
- 2D MRA synthesis is carried out in every channel.
- The image at various resolution levels are found. Add the images at all levels, the result is a ROI reconstructed image.

3.3 Mutiresolution Reconstruction Using 1D Wavelets

In [11] Peyrin *et.al.* studied the reconstruction of tomographic images from the one-dimensional wavelet transform of its projections. They achieved this in Fourier domain only. They proved that, the reconstructed image from the wavelet transform (at a fixed scale) of the the projections is the two-dimensional wavelet transform of the original image at that scale. A modified proof is also given in [12]. This result is important because it gives the procedure to construct a two-dimensional wavelet function from the one-dimensional wavelet function. We use this theory in the algorithm developed in this thesis.

The two-dimensional wavelet function constructed by inverse Radon transforming the one-dimensional wavelet function is different from the conventional separable wavelet functions used for images. It is isotropic in frequency domain and non-separable. The implementation scheme given in [11] is reproduced here.

- For an assumed one-dimensional wavelet function, a two-dimensional wavelet function is found using the Fourier transform method.
- The Fourier transform of the projections are taken.
- The projections are multiplied with the wavelet function in Fourier domain to find the wavelet transforms of the projections.
- Using Fourier domain reconstruction the wavelet transformed projections are inverse Radon transformed.

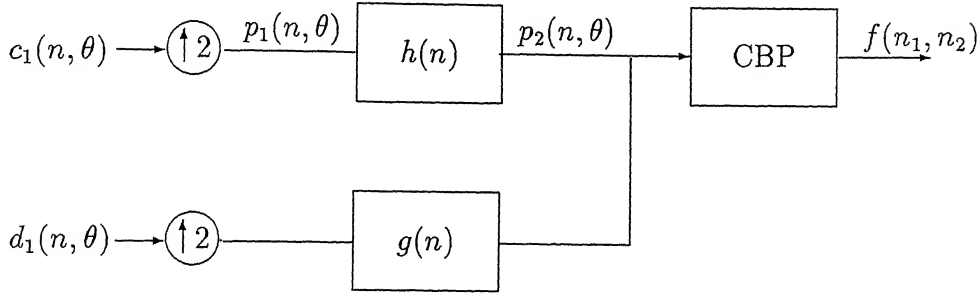


Figure 3.4: A simple combination of 1D MRA and CBP.

- The output is multiplied with the two-dimensional wavelet function in Fourier domain to find the images at various resolution levels.

3.4 1D MRA in Multiresolution Reconstruction

In this section using the proof given in [11] a new algorithm is proposed and discussed. Unlike the work described by Delaney in [10], the proposed method primarily uses the 1D-MRA analysis of the projections. At the synthesis end, the convolution backprojection operator is applied before the synthesis filters, in each channel respectively. As an example a simple one level MRA decomposition is taken to prove the result. Then the scheme is extended for higher level of decompositions.

3.4.1 Single Level MRA With CBP

As shown in Fig. 2.3, the projection $p(s, \theta)$ is first given as an input to a single level one-dimensional MRA filter bank. The decomposed signals, $c_1(n, \theta), d_1(n, \theta)$ are used as inputs to the synthesis stage as shown in Fig. 3.4. Since multiresolution analysis and synthesis gives perfect reconstruction the $p(s, \theta)$ will be exactly reconstructed at the synthesis end. Define a two-

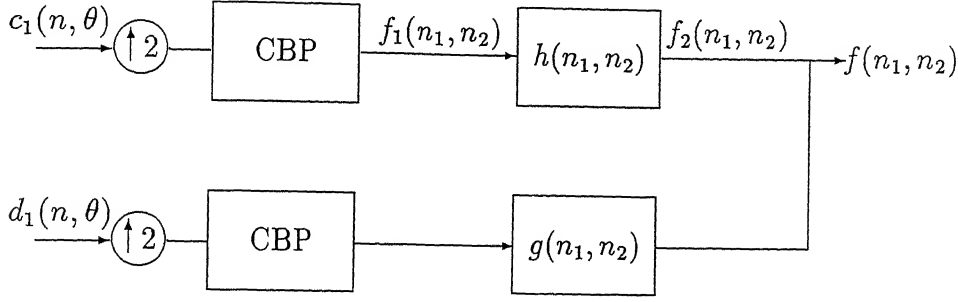


Figure 3.5: Modification of the simple ‘MRA-CBP’ combination by moving CBP inside.

dimensional function $h(n, \theta)$ as

$$h(n, \theta) = h(n) \quad \text{for every } \theta, \quad (3.10)$$

The synthesis equation can be written as

$$p_2(n, \theta) = p_1(n, \theta) \otimes_{1d} h(n, \theta) \quad (3.11)$$

By convolution property of Radon transform we have,

$$f_2(n_1, n_2) = f_1(n_1, n_2) \otimes_{2d} h(n_1, n_2) \quad (3.12)$$

Similarly, in other channels, the convolution backprojection operator is also moved in before the synthesis filters. The modified implementation scheme is shown in Fig. 3.5.

3.4.2 Determination of 2D filters

Though the two-dimensional filters are inverse Radon transform of the corresponding one-dimensional filters, the straight forward implementation of convolution backprojection on one-dimensional filters will result in filters having extremely poor frequency response, because of reduced number of samples. Here we propose an alternative scheme, described below.

- From $h(n)$ and $g(n)$ find the corresponding one-dimensional wavelet and scaling functions using eqn. (2.24). This can be done at any required sampling rate depending on the accuracy needed.

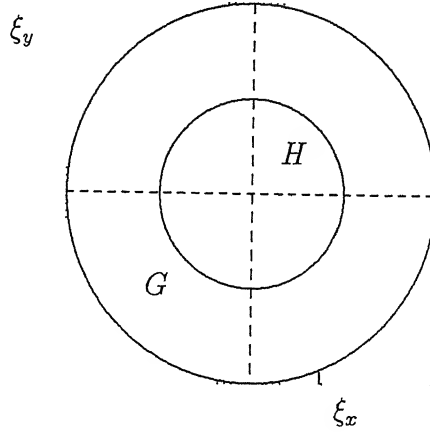


Figure 3.6: Tiling of the frequency plane by the constructed 2D wavelet transform.

- Find the two-dimensional wavelet and scaling functions by inverse Radon transforming the one-dimensional wavelet and scaling functions respectively.
- Find the two-dimensional filters using

$$h(n_1, n_2) = \iint \phi_{2d}(x, y) \phi_2(2x - n_1, 2y - n_2) dx dy \quad (3.13)$$

$$g(n_1, n_2) = \iint \psi_{2d}(x, y) \phi_2(2x - n_1, 2y - n_2) dx dy \quad (3.14)$$

This is done only once in the entire process of first reconstruction. After that for repeated reconstruction, for the same wavelet function, we use the same filters.

3.4.3 Properties of the Constructed 2D filters

As mentioned before the properties of the two-dimensional filters affect the performance of region of interest reconstruction. Since $h(n_1, n_2)$ is inverse Radon transform of $h(n)$ we can perceive it as an isotropic lowpass filter. Similarly $g(n_1, n_2)$ has the passband as shown in Fig. 3.6. We note that $g(n_1, n_2)$ is zero at the origin and in the neighbourhood in the Fourier domain. From the discussion given earlier, if $|\xi| \hat{W}(\xi)$ is combined with this filter, it

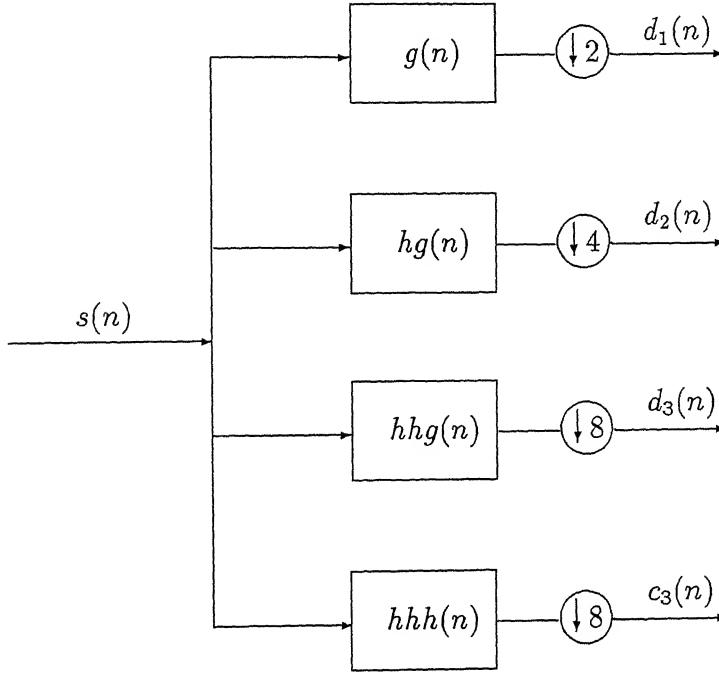


Figure 3.7: An equivalent implementation of MRA.

will result in a smaller length filter. This is the major advantage of this modified technique.

3.4.4 Higher level Decomposition

Consider the MRA synthesis filter bank shown in Fig. 2.4. The convolution backprojection operator cannot be shifted before the upsampling operations. So we face difficulties at higher level of decompositions. Let us view this problem in the analysis domain. Consider a three level analysis filter bank for the one-dimensional MRA. The filters which are present after the downsampling, can be placed before the downsampling block, thereby resulting in upsampling this filter. The modified analysis filter bank is shown in Fig. 3.7. But in the two-dimensional case, as explained earlier, we need an explicit expression to calculate two-dimensional filter from the two-dimensional wavelet and scaling functions. Using the theory of multiresolution analysis, the filters

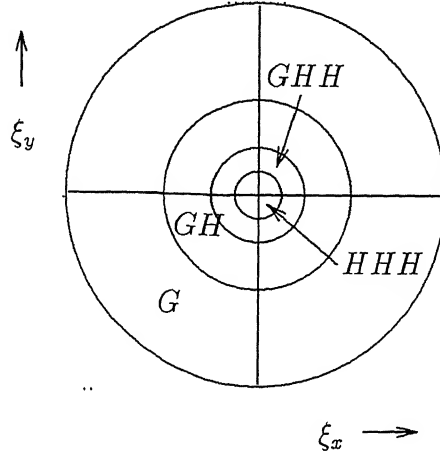


Figure 3.8: Tiling of the frequency plane by the constructed 2D wavelet transform.

can be obtained using the equations

$$h_k(n) = \int \phi_{1d}(t) \phi_{1d}(2^k t - n) dt \quad (3.15)$$

$$h_{k-1}g(n) = \int \psi_{1d}(t) \phi_{1d}(2^k t - n) dt \quad (3.16)$$

This can be extended to two-dimension as

$$h_k(n_1, n_2) = \iint \phi_{2d}(x, y) \phi_{2d}(2^k x - n_1, 2^k y - n_2) dx dy \quad (3.17)$$

$$h_{k-1}g(n_1, n_2) = \iint \psi_{2d}(x, y) \phi_{2d}(2^k x - n_1, 2^k y - n_2) dx dy \quad (3.18)$$

The passband characteristics of the two-dimensional filters are shown in Fig. 3.8. The convolution backprojection can now be carried out before the filtering operation. The modified implementation scheme for a three level multiresolution reconstruction is shown in Fig. 3.9.

3.4.5 Region of Interest Reconstruction

Referring to Fig. 3.8 we observe that the filters $h_{k-1}g(n_1, n_2)$ have zero value at the origin as well as in the neighborhood of the origin. So if we can combine $|\xi| \hat{W}(\xi)$ with these functions in the two-dimensional case, we can obtain short length filter. The convolution backprojection operation can be

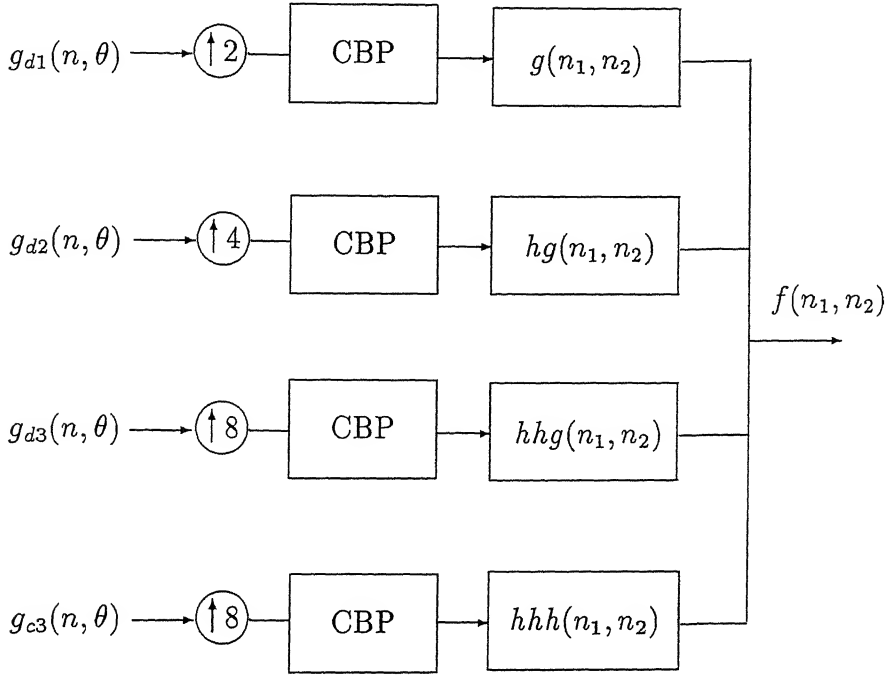


Figure 3.9: Multiresolution reconstruction for three level MRA.

represented as two blocks, first is the convolution with $|\xi|\hat{W}(\xi)$ and next is backprojection operation. Using the convolution property of the Radon transform we prove here that the one-dimensional filter which is an integral part of convolution backprojection can be moved over the backprojection block, resulting in a two-dimensional filtering with the inverse Radon transform of the one-dimensional filter. Consider the convolution backprojection equation

$$f(x, y) = \int p(s, \theta) \otimes_{1d} \text{IFT}_{1d} \{ |\xi| \hat{W}(\xi) \} d\theta \quad (3.19)$$

$$= \int \text{IFT}_{1d} \{ \hat{p}(\xi, \theta) \} \otimes_{1d} \text{IFT}_{1d} \{ |\xi| \hat{W}(\xi) \} d\theta \quad (3.20)$$

$$= \int \text{IFT}_{1d} \left\{ \frac{\hat{p}(\xi, \theta)}{|\xi| \hat{W}(\xi)} |\xi| \hat{W}(\xi) \right\} \otimes_{1d} \text{IFT}_{1d} \{ |\xi| \hat{W}(\xi) \} d\theta \quad (3.21)$$

$$= \int \left[\text{IFT}_{1d} \left\{ \frac{\hat{p}(\xi, \theta)}{|\xi| \hat{W}(\xi)} \right\} \otimes_{1d} \text{IFT}_{1d} \{ |\xi| \hat{W}(\xi) \} \right] \otimes_{1d} \text{IFT}_{1d} \{ |\xi| \hat{W}(\xi) \} d\theta \quad (3.22)$$

Equation (3.23) is the inverse Radon transform of one-dimensional convolution of two functions. Applying the convolution property of Radon transform it can be written as,

$$f(x, y) = \left[\int \text{IFT}_{1d} \left\{ \frac{\hat{p}(\xi, \theta)}{|\xi| \hat{W}(\xi)} \right\} \otimes_{1d} \text{IFT}_{1d} \{ |\xi| \hat{W}(\xi) \} d\theta \right] \otimes_{2d} \left[\int \text{IFT}_{1d} \{ |\xi| \hat{W}(\xi) \} \otimes_{1d} \text{IFT}_{1d} \{ |\xi| \hat{W}(\xi) \} d\theta \right] \quad (3.23)$$

$$f(x, y) = \left[\int p(s, \theta) d\theta \right] \otimes_{2d} \left[\sqrt{\xi_x^2 + \xi_y^2} \hat{W}_{2d}(\xi_x, \xi_y) \right] \quad (3.24)$$

where

$$\hat{W}_{2d}(\xi_x, \xi_y) = \hat{W}(\xi = \xi_x \cos \theta + \xi_y \sin \theta).$$

Using this approach we combine the $|\xi| \hat{W}(\xi)$ in the two-dimension with the two-dimensional synthesis filters. This combination is advantageous only when it is combined with highpass or bandpass filters. Further more it gives computational disadvantage with lowpass filter. Since the two-dimensional filter is non-separable, the filtering in two-dimension is computationally intensive than than filtering in one-dimension. Since the conversion of $|\xi| \hat{W}(\xi)$ to two-dimension in one channel is independent of the other channels, this is not done in lowpass channel to avoid the computational cost. The Implementation algorithm is clearly shown in the Fig. 3.10.

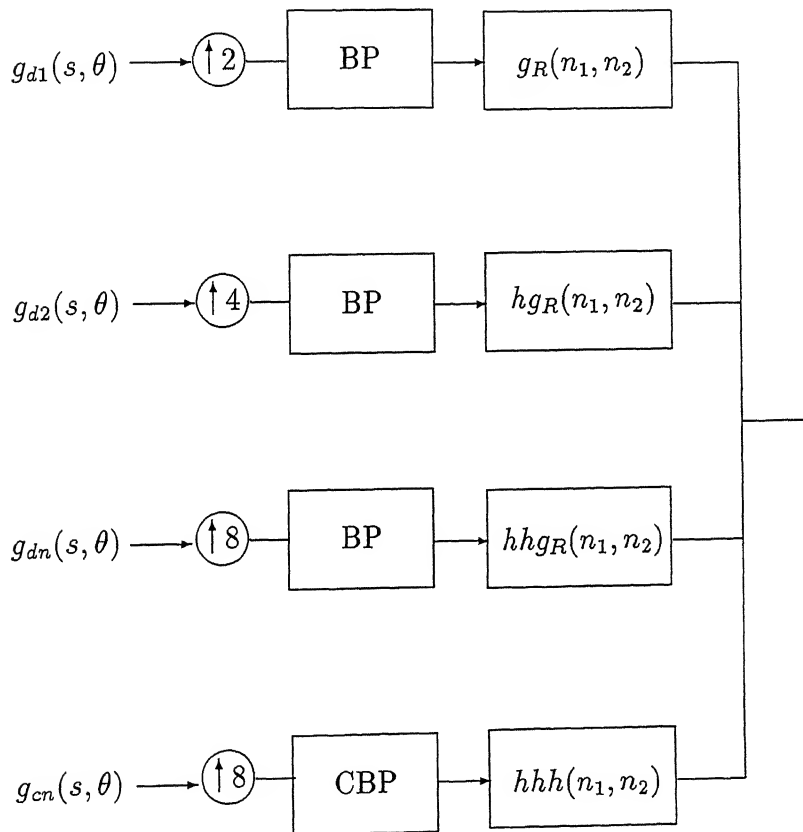


Figure 3.10: Region of reconstruction for three level MRA.

Chapter 4

Implementation and Discussions

The algorithm is implemented using Daubechies ten compactly supported orthonormal wavelets. The projections are simulated for the head phantom(Fig. 4.4). The results are given in the section 4.1. A brief discussion on the results is given in ???. A comparison of the new algorithm with other algorithms is given in section 4.3.

4.1 Simulation Results

The implementation scheme for multiresolution reconstruction is shown Fig. 3.9 and the region of interest reconstruction in Fig. 3.10.

As discussed, the one-dimensional scaling function and wavelet are inverse Radon transformed to obtain the two-dimensional scaling function and wavelet. Using eqn. (3.18), $h(n_1, n_2)$ and $g(n_1, n_2)$ are obtained. To our surprise the filter responses are not what we expected or rather what is given in theory. This is due to the non-alignment of center of projections in the inverse Radon transform operation. To explain briefly, the center point of the projections should be aligned in backprojection, otherwise the function in two-dimension cannot be reconstructed exactly.

To align the centers, zeropadding of the sequence is carried out and the

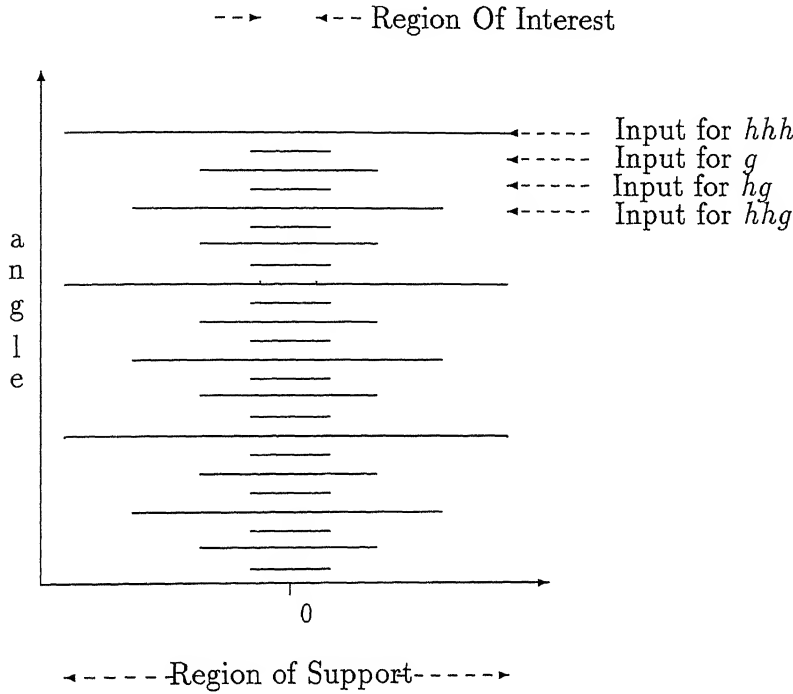


Figure 4.1: Sampling scheme for the region of interest reconstruction inputs.

two-dimensional scaling function and wavelet are found. To illustrate this effect, for a misaligned scaling function, inverse Radon transform is taken to find the $h(n_1, n_2)$. The frequency response of this filter is shown in Fig. ???. To center them, we used 197 zeros padded on the left of scaling function and 16 zeros padded on the left of wavelet. This is found by repeated trials, to make the Fourier transform of the two-dimensional filters' cross section correspond to one-dimensional filter response. The one-dimensional filters' responses are shown in Fig. 4.5 and the two-dimensional filters' responses are shown in Figs. 4.7 to 4.10. Since the convolution of projections with MRA filters introduce noninteger phase shift, the origin of the projections is shifted and the zeropadding procedure cannot solve this as the shift is a noninteger. The effect of this noninteger phase shift on the reconstructed image is illustrated for Shepp-Logan head phantom using conventional convolution backprojection operator is shown in Fig. 4.11. To correct this problem, an offset value is added with the $s = x \cos \theta + y \sin \theta$. The simulation results on Shepp-Logan head phantom are shown in Fig. 4.20-4.24.

For region of interest reconstruction the scheme shown in Fig. 3.10 is implemented. The projections corresponding to a reduced number of angles are given input to the lowpass channel and the input to the other channels are illustrated clearly in Fig. 4.1. The region of interest reconstruction filter frequency responses are shown in Fig. 4.17-4.19. Simulation results are shown in Fig. 4.20-4.24. The simulation results, to demonstrate that the offcentered region of interest reconstruction is also possible, are shown in Fig. 4.25 to 4.28.

4.2 Discussions

As we stated previously, the new algorithm for region of interest image reconstruction from projections work fairly well at resolution levels 2^{-1} and 2^{-2} . The edge information on these levels are fairly acceptable. The images at resolution levels 2^{-3} however is blurred as expected. The same is true for region of interest reconstructed images at various levels.

The limitations of the algorithm are twofold.

- The process of finding the two dimensional filters requires inverse Radon transforming the scaling and wavelet functions respectively. An alignment of the centers for all angles has to be carried out before inverse Radon transforming.
- As the one-dimensional multiresolution analysis filters introduce non-integer phase delays on the projections, an offset is added while taking the inverse Radon transform.

4.3 Comparison of the Algorithms

As discussed earlier, Olson's algorithm, given in [9], is inferior in many aspects as given in [10], we compare here our algorithm only with the results reported in [10].

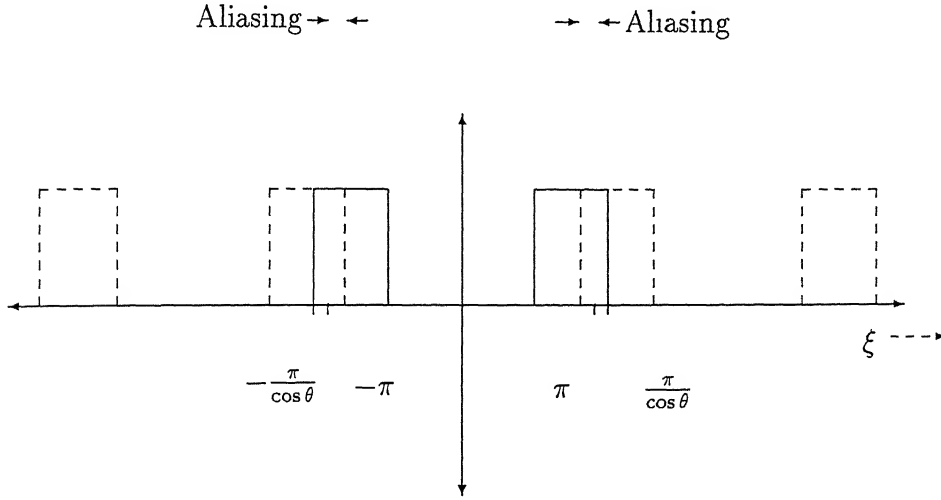


Figure 4.2: The aliasing effect produced in 2D MRA reconstruction for a particular angle θ .

4.3.1 Aliasing effect

The Delaney's algorithm gives aliasing at high frequencies thereby degrading the image. This is due to the fact that the one-dimensional discrete frequency is restricted between $-\pi$ to π . This can be explained from the frequency response plot of the two-dimensional MRA filters and its Radon transformed one-dimensional MRA filters. This is shown in the Fig. 4.3 and the aliasing effect for a single filter at an angle θ is shown in Fig. 4.2. In lowpass filters no aliasing occurs. But in highpass filters when the projection angle is not equal to 0 or $\pi/2$ the two-dimensional frequency plane extends from $-\pi/\cos \theta$ to $\pi/\cos \theta$ for $\theta < \frac{\pi}{4}$ (and for $\theta < \frac{\pi}{4}$ frequency plane is from $-\pi/\sin \theta$ to $\pi/\sin \theta$). Since this is greater than the span from $-\pi$ to π , the aliasing effect comes.

As the images in general have very low power in the high frequency components, this was not observed in the results reported in [10]. In the proposed algorithm, as the synthesis filters are the inverse Radon transform of the one-dimensional filters, the synthesis filters have zero outside the circle of radius π in two-dimensional frequency plane. This proves that the developed algorithm according to theory will give better results.

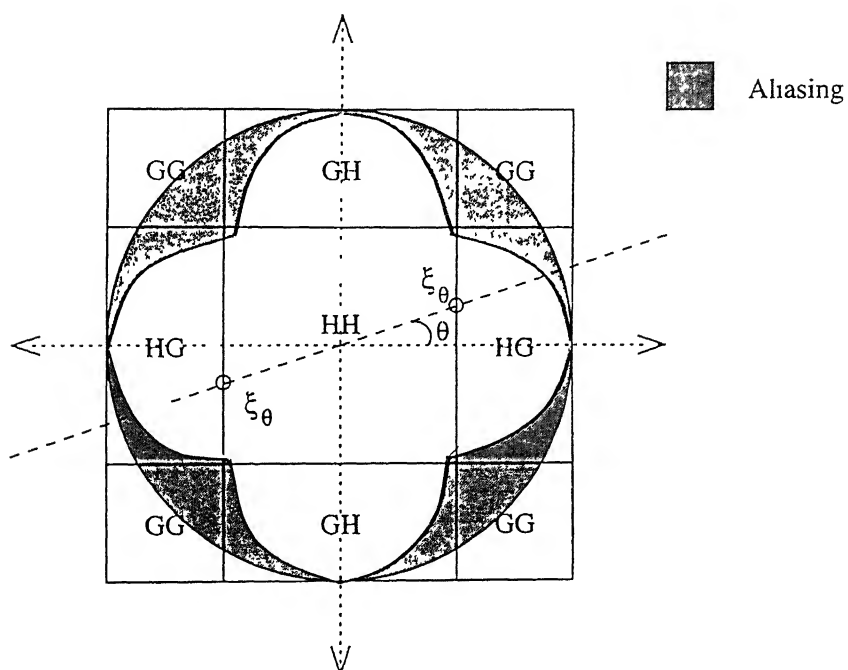


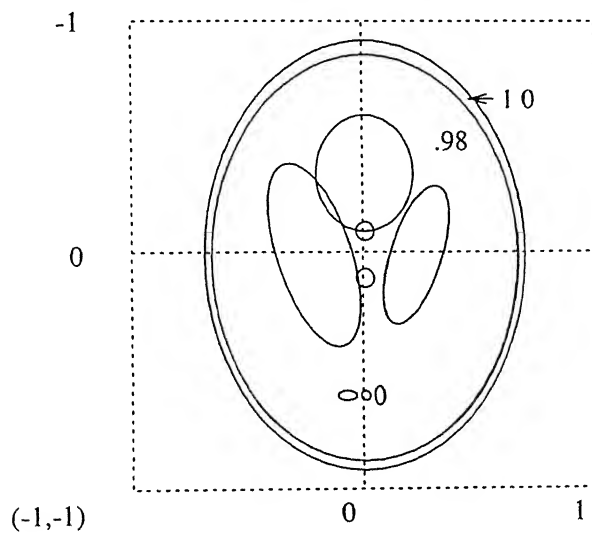
Figure 4.3: The aliasing effect produced in 2D MRA reconstruction shown in two-dimensional frequency plane.

4.3.2 Computational Complexity

Designing the two-dimensional filters is computationally very intensive, as we need to find inverse Radon transform of the fine sampled scaling and wavelet functions. But this is to be done only once while setting up the algorithm. So this is not considered in the run time computational requirement calculations.

The MRA synthesis is done in the two-dimensional domain in which the filters are non-separable. So the number of computations is increased to $N^2 \times N_1^2$ whereas in separable filter implementation it is $N \times N_1$ (N is the length of the two-dimensional filter in both direction or one-dimensional filter length and N_1 is sequence length). As mentioned before the lowpass channel is not modified in region of interest reconstruction, from the multiresolution reconstruction algorithm. This significantly reduces the number of multiplications. The overall computational requirements for the multiresolution reconstruction is shown in Fig. 4.29. In that the number of samples considered for projections is 100 and number of angles considered is 128. The image is sampled in 256×256 grid and filtered. The computational requirements for region of interest reconstruction is shown in Fig. ???. The region of interest radius is 30 and the sampling scheme is shown in Fig. 4.1. The number of projection samples for lowpass filter is 256 and number of angles considered is 32. The image is sampled only in the region of interest.

Note : In two-dimensional frequency response plots, the first plot denoted as (a), is with the hidden surfaces and the second one in the same figure, denoted as (b), is without the hidden surfaces.



Phantom Head

All inner ellipses are with 0.5 density

Figure 4.4: Shepp-Logan Phantom head image used for simulations.

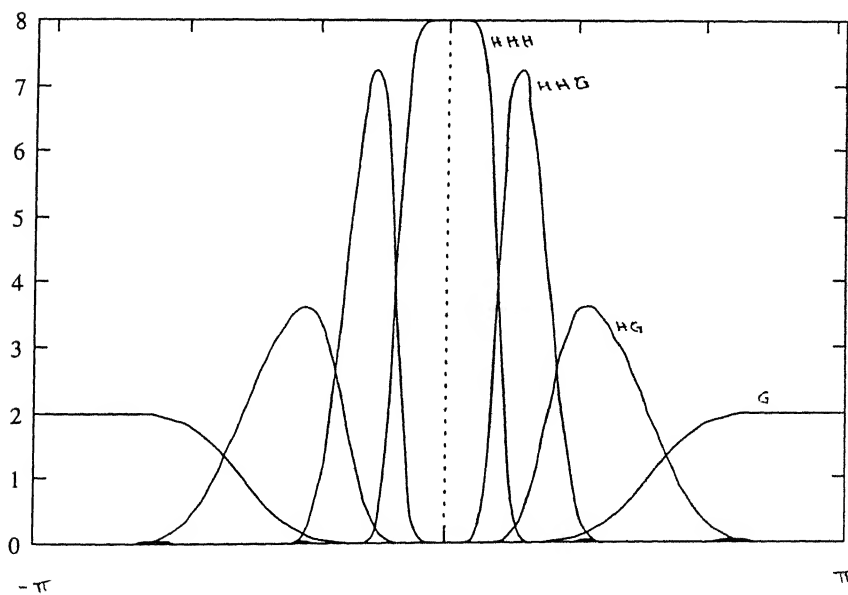


Figure 4.5: Frequency responses of the 1D analysis filters.

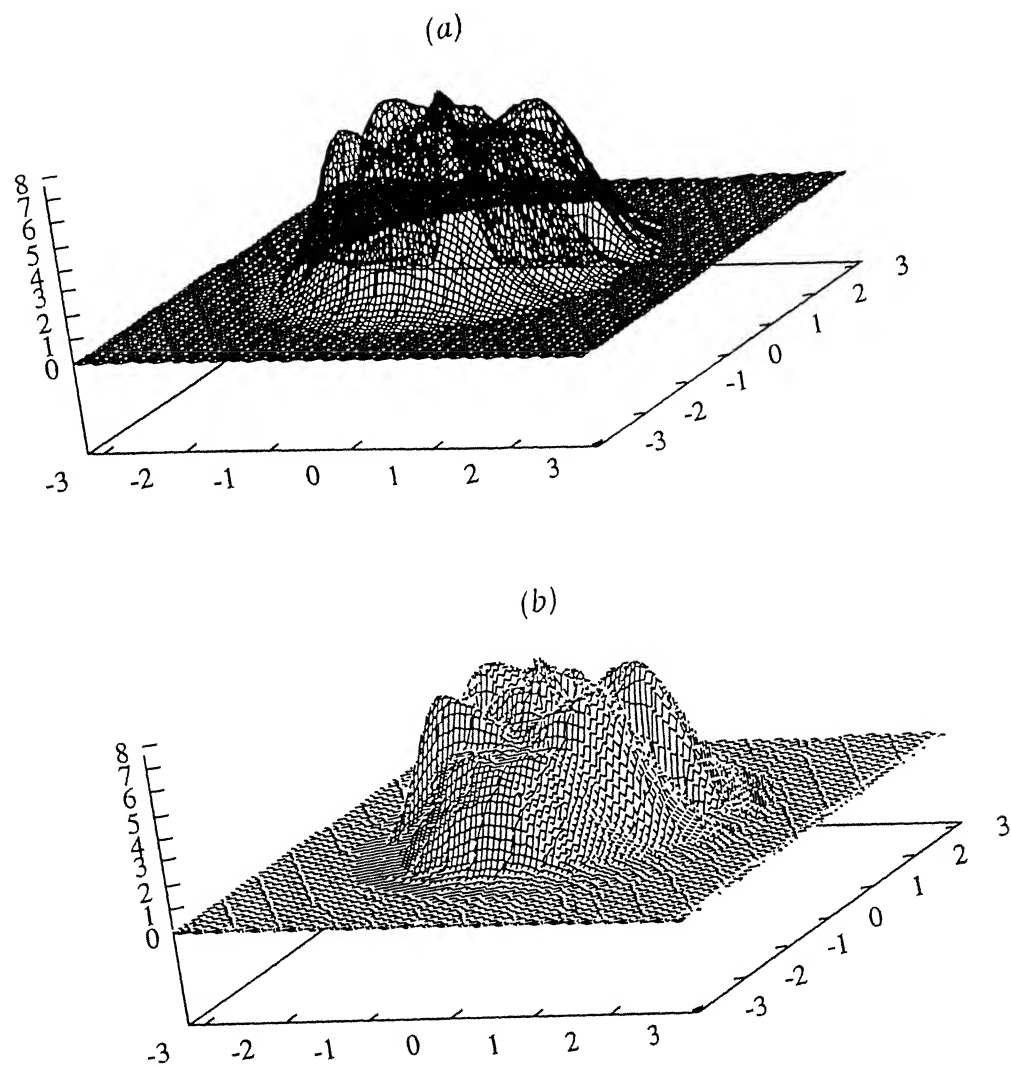


Figure 4.6: Frequency response of the 2D synthesis filter $h(n_1, n_2)$ constructed with misaligned scaling function.

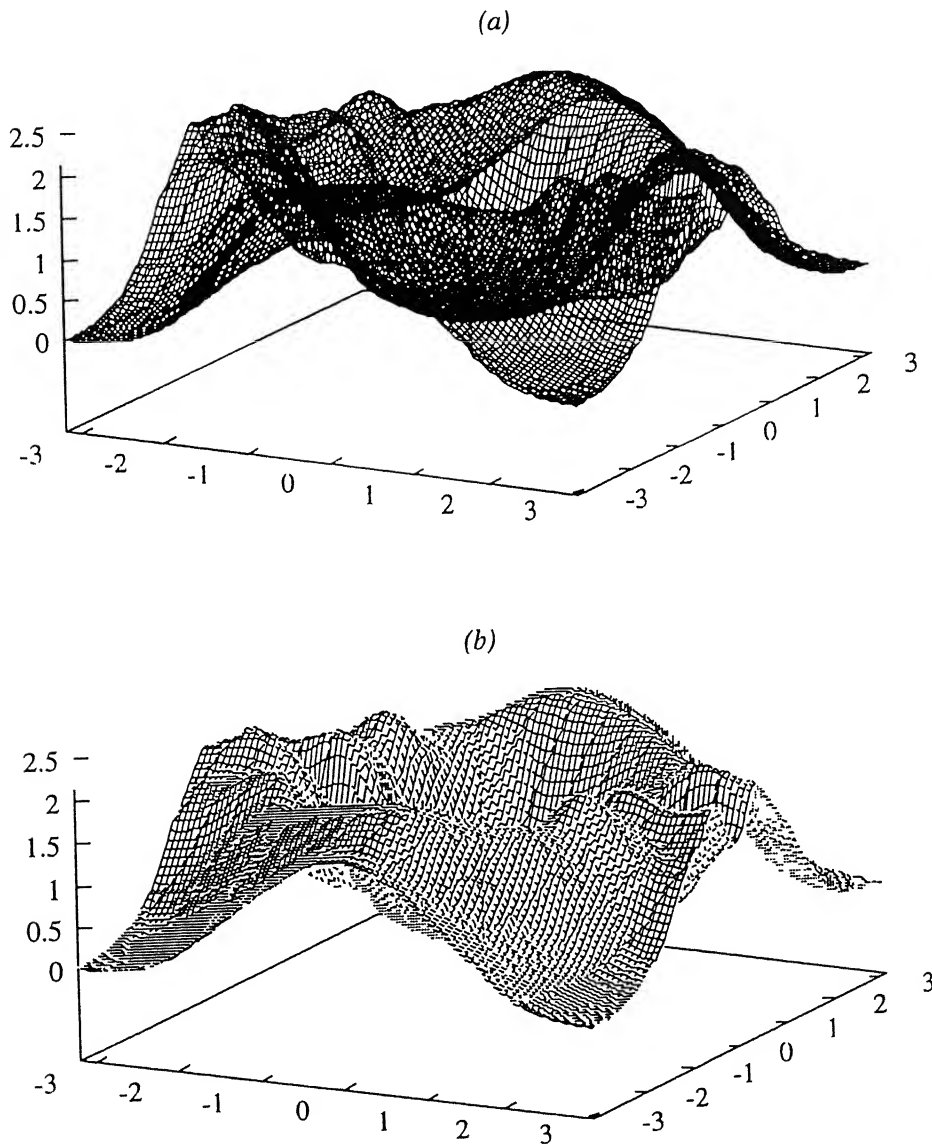


Figure 4.7: Frequency response of the 2D synthesis filter $g(n_1, n_2)$.

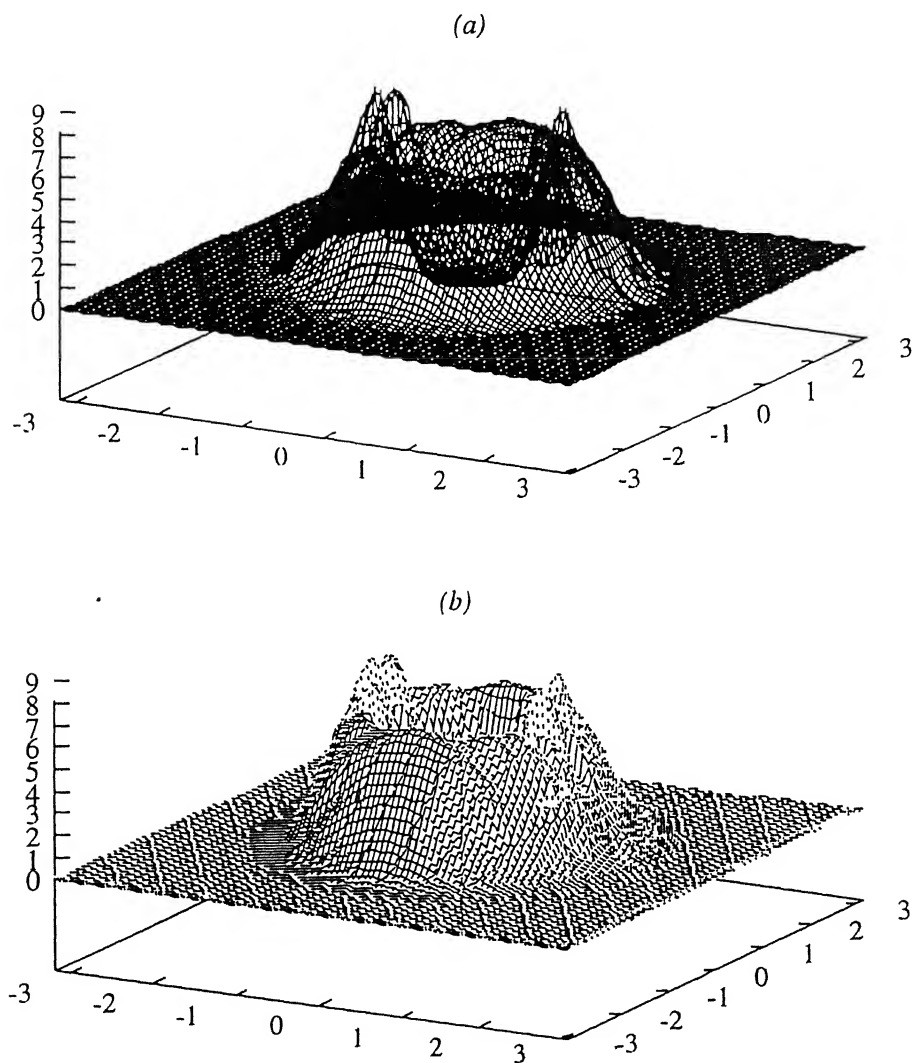


Figure 4.8: Frequency response of the 2D synthesis filter $hg(n_1, n_2)$.

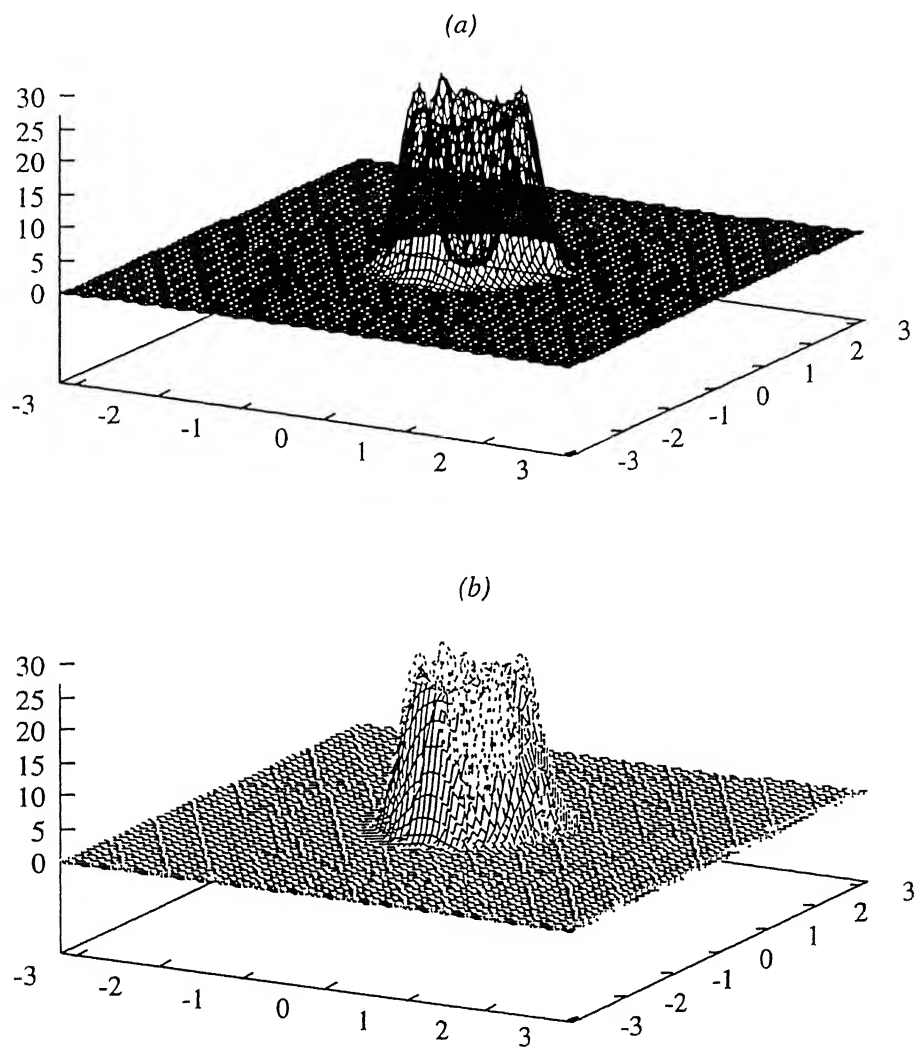


Figure 4.9: Frequency response of the 2D synthesis filter $hhg(n_1, n_2)$.

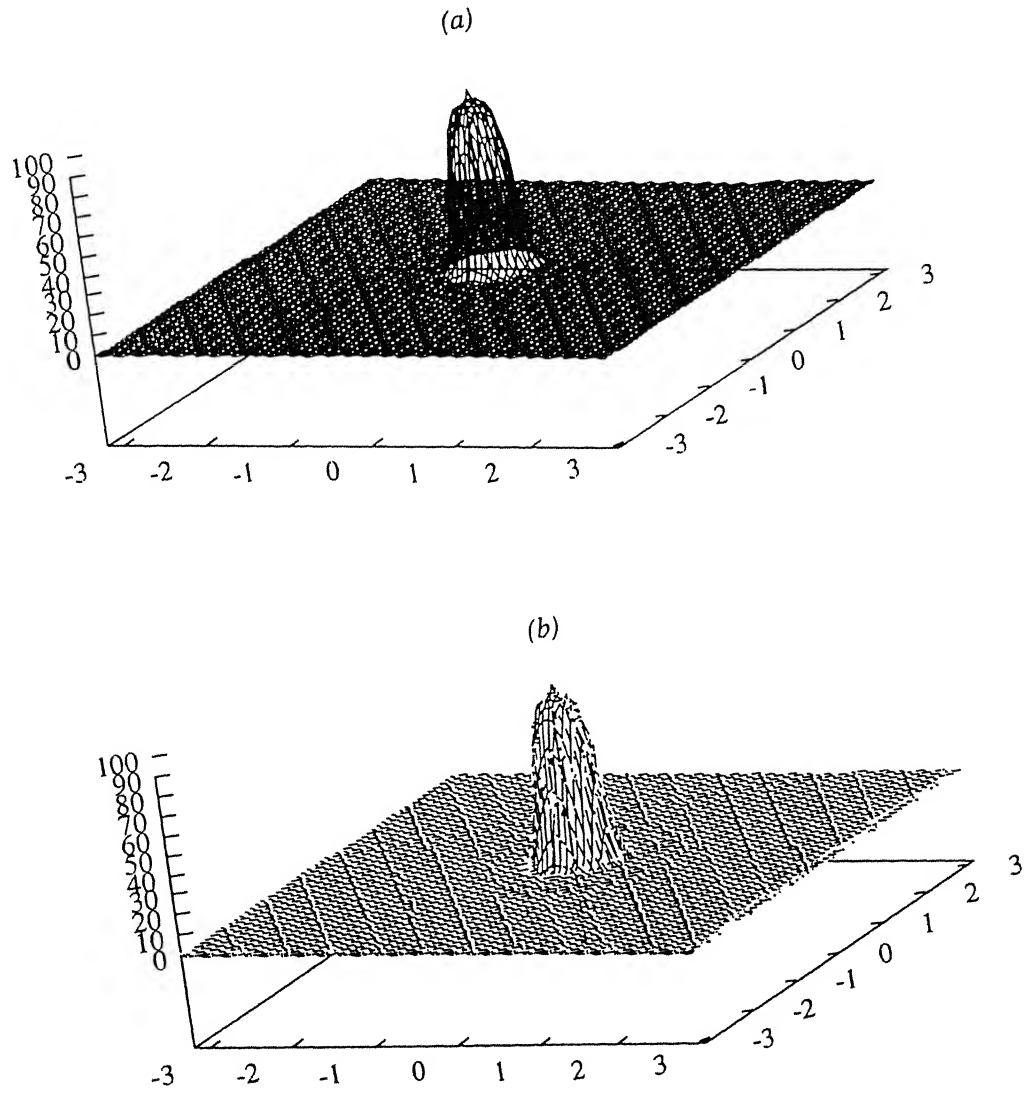


Figure 4.10: Frequency response of the 2D synthesis filter $hhh(n_1, n_2)$.

Figure 4.11: Illustration of the effect of misalignment of projection origin.

Figure 4.12: Multiresolution reconstruction: Image at resolution 2^{-1} .

Figure 4.13: Multiresolution reconstruction: Image at resolution 2^{-2} .

Figure 4.14: Multiresolution reconstruction: Image at resolution 2^{-3} .

Figure 4.15: Multiresolution reconstruction: Coarse image at resolution 2^{-3} .

Figure 4.16: Multiresolution reconstruction: Overall added image.

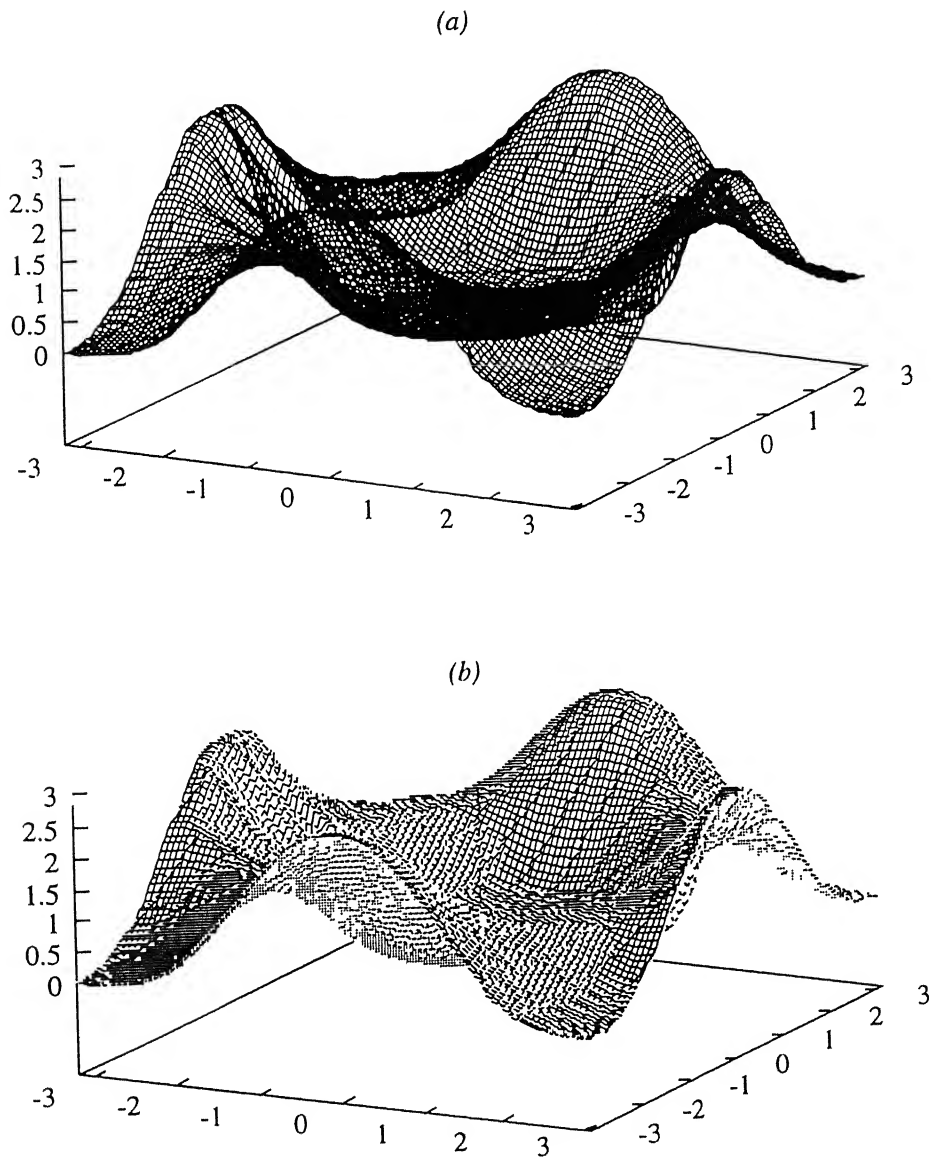


Figure 4.17: Frequency response of the 2D synthesis filter $g_R(n_1, n_2)$.

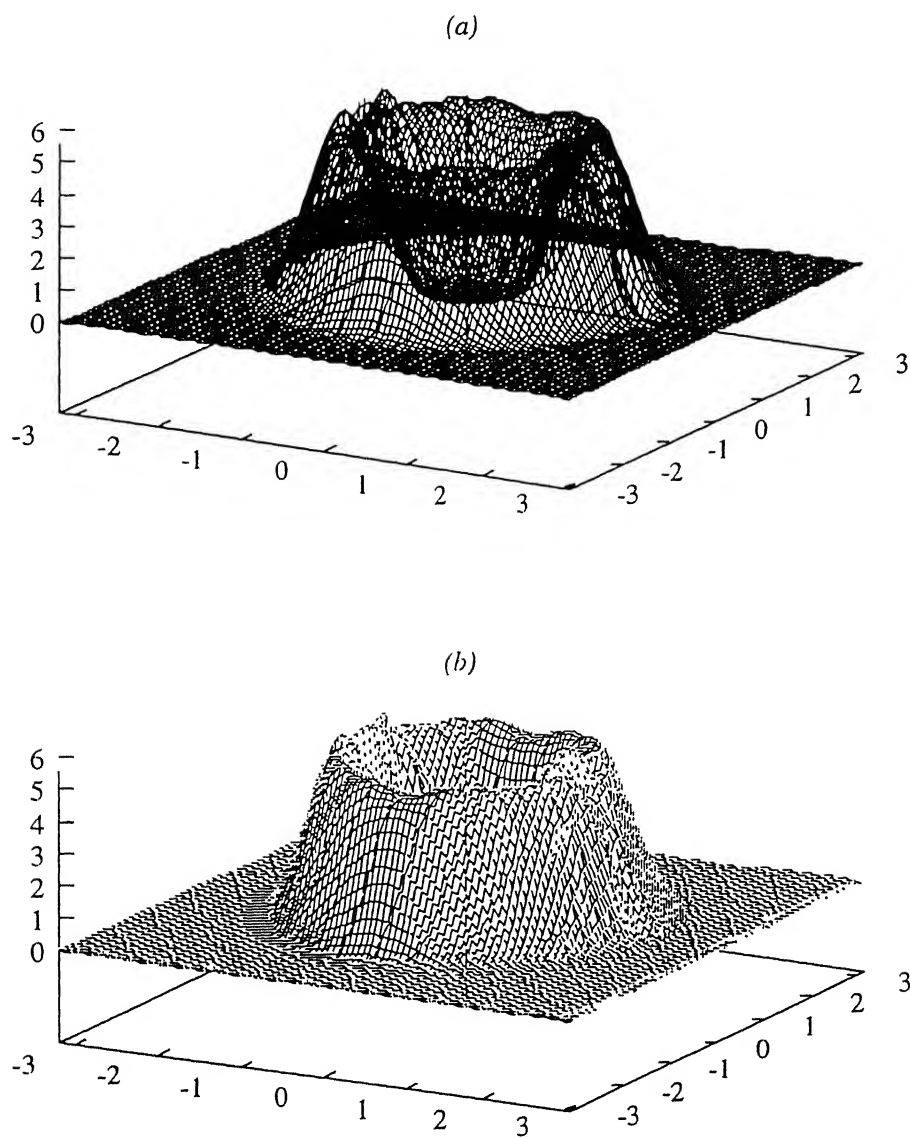


Figure 4.18: Frequency response of the 2D synthesis filter $hg_R(n_1, n_2)$.

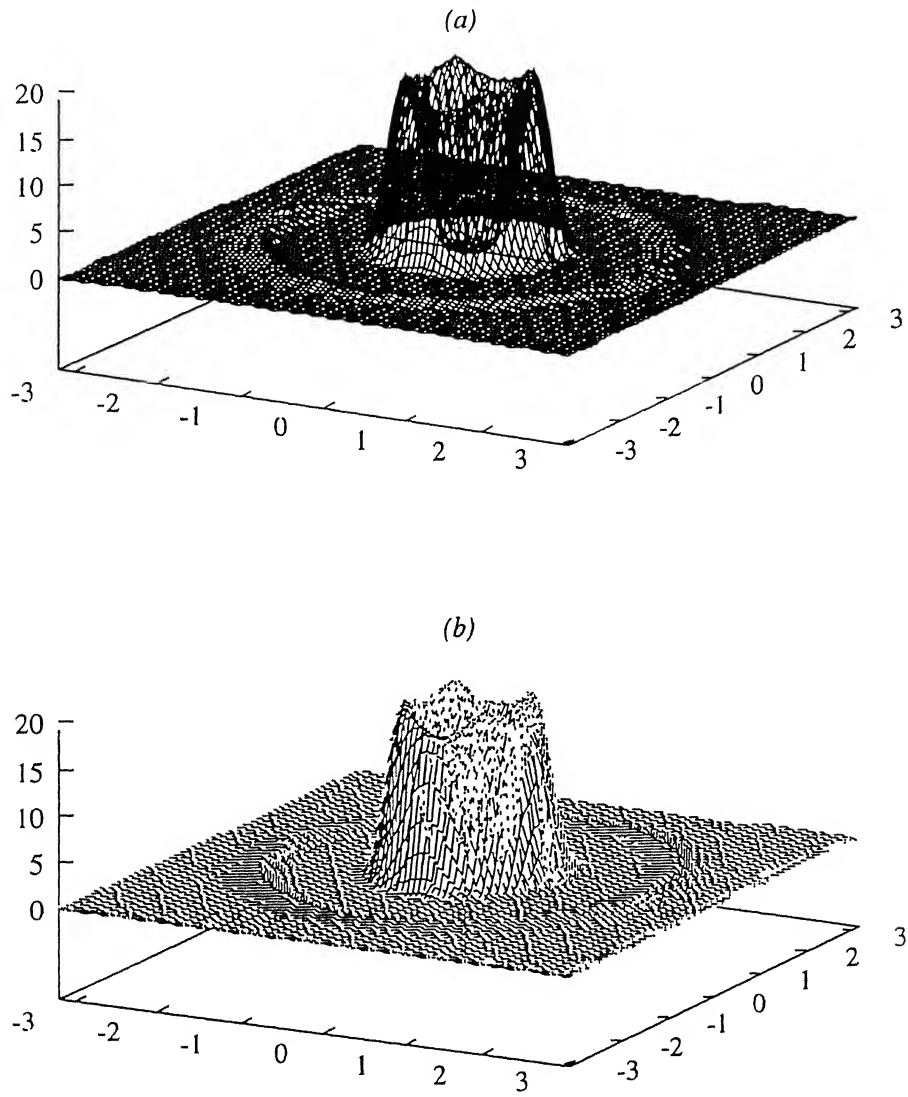


Figure 4.19: Frequency response of the 2D synthesis filter $hhg_R(n_1, n_2)$.

Figure 4.20: Centered region of interest image at resolution 2^{-1} .

Figure 4.21: Centered region of interest image at resolution 2^{-2} .

Figure 4.22: Centered region of interest image at resolution 2^{-3} .

Figure 4.23: Region of interest reconstruction. Coarse image at resolution 2^{-3} .

Figure 4.24: Overall added centered region of interest image.

Figure 4.25: Offcentered region of interest image at resolution 2^{-1} .

Figure 4.26: Offcentered region of interest image at resolution 2^{-2} .

Figure 4.27. Offcentered region of interest image at resolution 2^{-3} .

Figure 4.28: Overall added offcentered region of interest image.

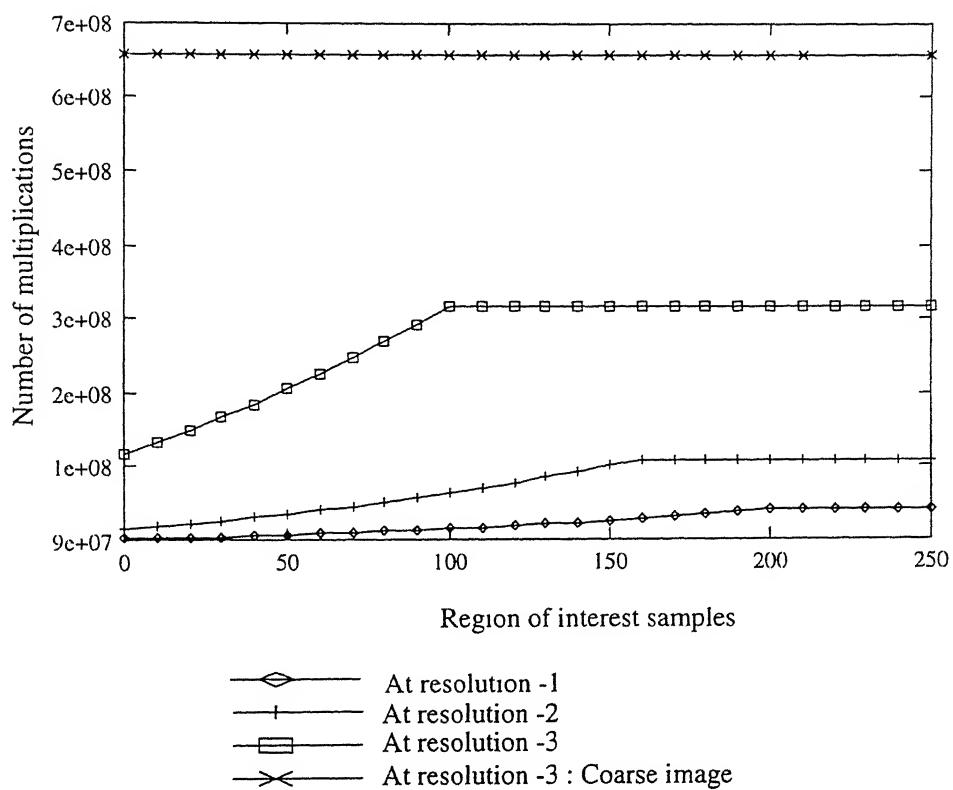


Figure 4.29: Computational requirements in number of multiplications for the varying region of interest samples.

Chapter 5

Conclusion

The objective of the thesis was to explore a new algorithm for region of interest image reconstruction. It has been found that the proposed algorithm is able to extract the edge information at resolution levels 2^{-1} and 2^{-2} . But the overall reconstruction is found to be visibly poorer than the conventional convolution backprojection method. This is due to the extensive operations done on the projection data and the inverse Radon transform of the signal which has $2^n - 1$ zeros at the n^{th} level. The aim of the algorithm developed was not solely to reconstruct the image from projections, but also to reduce the amount of radiation exposure, i.e. to use minimum number of projection samples. By combining the non-local filter with the two-dimensional synthesis filters the localization is achieved. The algorithm is also applicable for offcentered region of interest image reconstruction. the present algorithm does not have the aliasing error unlike the algorithm given in [10]. This is achieved at the cost of increased computations. The algorithm is found to be suitable for reconstructing the region of interest images at 2^{-1} and 2^{-2} resolution levels. This is because the image reconstruction at these levels needs less computation, at the same time gives the required edge information.

Bibliography

- [1] S.R. Deans, "The Radon Transform and some of its application", *Wiley Interscience Publication*, 1983.
- [2] A.K. Jain, "Fundamentals of Image Processing", *Prentice Hall International Inc.*, 1989.
- [3] I. Daubechies, "Ten Lectures on Wavelets", *Society for Industrial and Applied Mathematics*, 1992.
- [4] Yves Meyer, "Wavelets : Theory and Algorithms", *Society for Industrial and Applied Mathematics*, 1993.
- [5] Y.T. Chan, "Wavelet Basics", *Kluwer Academic Publishers*, 1995.
- [6] S. G. Mallat, "A Theory for Multiresolution Signal Decomposition : The Wavelet Representation", *IEEE Transaction on Pattern Analysis and Machine Intelligence*, Vol. 11, No. 7, Jul. 1989.
- [7] S. G. Mallat, "Multifrequency Channel Decomposition of Images and Wavelet Models", *IEEE Transaction on ASSP*, Vol. 37, No. 12, Dec. 1989.
- [8] O. Rioul, M. Vetterli, "Wavelets and Signal Processing", *IEEE Signal Processing Magazine*, Oct. 1991.
- [9] T. Olson, J. DeStefano, *Wavelet Localization of the Radon Transform*, *IEEE Transaction on Signal Processing*, Vol. 42., No. 8, Aug. 1994.
- [10] A.H. Delaney, Y. Bresler, "Multiresolution Tomographic Reconstruction Using Wavelets", *IEEE Transaction on Image Processing*, 1995.

-
- [11] F. Peyrin , M. Zaim and R. Goutte, "Construction of Wavelet Decompositions for Tomographic Images", *Journal of Mathematical Imaging and Vision*, Vol. 3, 1993.
 - [12] G. Varatharajan, "Image Reconstruction using Wavelets", M.Tech Thesis, Indian Institute of Technology, Kanpur, 1995.
 - [13] B. Sahiner, A. Yagle, "Time Frequency Distribution Inversion of the Radon Transform", *IEEE Transactions on Image Processing*, Vol. 2, No. 4, Oct. 1993.
 - [14] B. Sahiner, A. Yagle, "Image Reconstruction from Projections under Wavelet Constraints", *IEEE Transactions on Signal Processing*, Vol. 41, No. 12, Dec. 1993.
 - [15] B. Sahiner, A. Yagle, "Limited Angle Tomography using Wavelets", *IEEE Medical Imaging Conference*, 1993.
 - [16] B. Sahiner, A. Yagle, "Reconstruction from projections Under Time Frequency Constraints", *IEEE Transactions on Medical Imaging*, Vol. 14, No. 2, Jun. 1995.
 - [17] B. Sahiner, A. Yagle, "Region of Interest Tomography Using Exponential Radial Sampling", *IEEE Transactions on Image Processing*, Vol. 4, No. 8, Aug. 1995.
 - [18] A. Yagle, "Region of Interest Tomography Using the Wavelet Transform and Angular Harmonics", *IEEE Signal Processing Letters*, Vol. 1, No. 9, Sep. 1994.